Heat Transfer in Gold Interfaces Capped with Thiolated Polyethylene Glycol: A Molecular Dynamics Study

Sydney A. Shavalier and J. Daniel Gezelter*

251 Nieuwland Science Hall, Department of Chemistry and Biochemistry,
University of Notre Dame, Notre Dame, Indiana 46556

E-mail: gezelter@nd.edu

Abstract

Reverse non-equilibrium molecular dynamics (RNEMD) simulations were used to study heat transport in solvated gold interfaces which have been functionalized with a low molecular weight thiolated polyethylene glycol (PEG). The gold interfaces studied included (111), (110), and (100) facets, as well as spherical nanoparticles with radii of 10 and 20 Å. The embedded atom model (EAM) and the polarizable density-readjusted embedded atom model (DR-EAM) were implemented to determine the effect of metal polarizability on heat transport properties. We find that the interfacial thermal conductance values for thiolated PEG capped interfaces are higher than those for pristine gold interfaces. Hydrogen bonding between the thiolated PEG and solvent differs between planar facets and the nanospheres, suggesting one mechanism for enhanced transfer of energy, while the covalent gold sulfur bond appears to create the largest barrier to thermal conduction. Through analysis of vibrational power spectra, we find an enhanced population at low frequency heat carrying modes for the nanospheres, which may also explain the higher mean G value.

Introduction

The unique optical properties of gold nanostructures make them useful candidates for biomedical applications such as photothermal therapies.[1–6] The localized surface plasmon resonance allows excitation of conduction band electrons upon irradiation with light at the same frequency as the plasmon resonance, giving gold nanostructures the ability to absorb light at particular wavelengths in the near IR.

Due to their similarities to sulfur-containing biological molecules, thiols and thiolates that functionalize gold nanoparticles have been studied extensively.[7–12] The thiol functional group is present in the amino acid cysteine, and cysteine adsorption onto gold has been studied both computationally[13–15] and experimentally.[14,16] Upon reaction with colloidal gold, thiols have been shown to bind to the gold via a strong S-Au bond, releasing hydrogen gas by breaking the S-H bond. In one study, the presence of hydrogen gas was confirmed using gas chromatography.[17] Alternatively, thiolate-capped gold nanoparticles can be synthesized via a ligand exchange reaction[18] or a two phase reduction.[19] For this work, we are concentrating on a low molecular weight thiolated polyethylene glycol (PEG) as a ligand. PEG is a biocompatible, water-soluble polymer with a molecular length that can be tailored for a variety of uses, notably as a bioconjugation agent.[20] The transfer of heat through nanomaterials functionalized with thiolated PEG is important in potential application to both photothermal and gene therapies.[21–23]

Significant experimental[24] and simulation studies[25–29] have contributed to our current understanding of heat transfer through thiolate-capped gold interfaces. Using time-domain thermoreflectance, Harikrishna *et al.* determined the interfacial thermal conductance (G) from a planar gold film capped with a variety of alkanethiol self-assembled monolayers (SAMs) which were solvated in water. They concluded that varying the terminal group of the alkanethiols changed the conductance, but the change could also be caused by the ability of water molecules to penetrate between the alkanethiol chains.[24] Their measured values of G were supported by molecular dynamics (MD) simulations of the same systems by Hung *et al.*[30] They found that the crowding of water molecules between the alkanethiols did indeed influence G, suggesting that it could be tuned by controlling, either via the terminal functional group or the SAM binding density, the ability of water to aggregate near the terminal end of the ligands.[30]

There is significant debate over how the size of a solvated gold nanosphere influences thermal transport due to changes in surface curvature. Tascini *et al.*[31] and Jiang *et al.*[32] determined that in systems of Lennard-Jones spherical nanoparticles solvated in a Lennard-Jones fluid, G increased with decreasing particle size. The prevailing argument for this trend is that the increase in undercoordinated surface atoms in smaller nanospheres creates a larger angle of contact between the surface atoms and the surrounding solvent. However, a study of gold nanospheres solvated in hexane concluded that while G increased from a flat Au(111) surface to spherical particles, there was very little size dependence over a range of particle radii from 20 Å - 40 Å.[33] Additionally, a study of gold nanoparticles capped with various alkanethiolates and solvated in hexane found that ligand structure and rigidity had a larger effect on the value of G than the size of the particle core.[26] In studies of pristine spherical gold nanoparticles solvated in water, the increase in conductance due to gold surface curvature was explained by the increase in the number of water molecules (energy carriers) close to the gold surface.[34–36] These results suggest that all three effects; coordination number of surface gold atoms, metal-to-ligand coupling, and metal-to-solvent interactions may impact interfacial thermal conductance.

Simulations of heat conduction through flat Au(111)-hexane interfaces with mixed-chain alkanethiolate ligands showed that ligand chain alignment has a significant impact on interfacial thermal conductance. Solvent molecule entrapment, in which hexane molecules were embedded between adjacent alkanethiolate ligands, substantially affected G. Orientational alignment between the solvent and ligand was found to increase thermal transfer from the ligand to the entrapped solvent molecules.[25] Stocker *et al.* and Harikrishna *et al.* separately determined via simulation[25] and experiment[24] that interfacial thermal conductance is not directly dependent on the ligand chain length in systems containing thiolate-capped gold. This can potentially be explained by ballistic heat transport through the ligand chains on the metal surface.[37]

Few previous simulation studies have considered the role that metal polarizability plays in these thermal transport processes. In this work, we utilize the density-readjusted embedded atom model (DR-EAM) from Bhattarai *et al.*,[38] which is a polarizable metal potential. The metal charges are propagated along with the atomic positions and velocities in simulations where DR-EAM is implemented. Two previous studies[39,40] found that G increases when DR-EAM is implemented in systems of pristine Au(111) solvated in water.

In this work, we have simulated thermal transport through planar Au surfaces and small Au nanospheres which have been capped with a fixed surface density of a low molecular weight thiolated PEG, $\mathrm{S(-CH_2CH_2O-)_3H}$. To study the effect of different surface facets, we used planar gold systems which expose the (100), (111), and (110) facets of crystalline gold to the ligand and solvent. Gold nanospheres ($r = 10$ Å and $r = 20$ Å) were simulated with the same surface ligand density, but they were encased in a solvent cloud rather than a periodic box. Details on the systems and the methods for generating thermal transport are presented in the following sections.

Methods

To simulate thermal transport, we utilized velocity shearing and scaling reverse non-equilibrium molecular dynamics (VSS-RNEMD).[41] In this method, an unphysical kinetic energy (or momentum) flux is applied by scaling (or shearing) particle velocities in two separated regions of the simulation. These regions are typically rectangular slabs in planar geometries and concentric spheres in the non-periodic geometries.[33] Temperature (or velocity) gradients form between the regions in response to the applied fluxes. To generate the fluxes, velocities are modified for particles i in the cold slab and particles j in the hot slab:

$$\mathbf{v}_i \leftarrow c \cdot (\mathbf{v}_i - \langle \mathbf{v}_c \rangle) + (\langle \mathbf{v}_c \rangle + \mathbf{a}_c) \tag{1}$$

$$\mathbf{v}_j \leftarrow h \cdot (\mathbf{v}_j - \langle \mathbf{v}_h \rangle) + (\langle \mathbf{v}_h \rangle + \mathbf{a}_h) \tag{2}$$

where $\langle \mathbf{v}_h \rangle$ and $\langle \mathbf{v}_c \rangle$ describe the instantaneous center of mass velocities for all molecules occupying the hot and cold slabs, respectively. At every timestep, velocities are scaled by two variables, h and c, while $\mathbf{a}_c$ and $\mathbf{a}_h$ are shearing terms that alter the relative mean velocities between the slabs. The applied flux values and conservation of energy and momentum provide simple solutions for the scaling (c and h) and shearing ($\mathbf{a}_c$ and $\mathbf{a}_h$) variables.

In standard NEMD methods, a gradient is applied using thermostats in two different regions, and a flux is calculated from the changes made to the velocities. In RNEMD methods, the flux is applied and the system's response (either a thermal gradient or temperature drop at an interface) is measured. In practice, either approach can be used with Fourier's law to compute thermal transport properties. However, applied flux methods like the one used here can be made to satisfy conservation of energy and linear momentum, and can be added to any molecular dynamics integration method.

The effects of gold morphology and surface polarizability on the solvent thermal conductivity and interfacial thermal conductance were investigated. We determined the organization of the ligand layer and its contact with both the metal and solvent, as well as the hydrogen bonding density between the ligand and solvent, the magnitude of metal-to-ligand and ligand-to-solvent coupling via Bhattacharyya coefficient calculations, and the vibrational power spectra.

Force Fields

For metallic interactions, we used the embedded atom model (EAM) parameterized by Zhou *et al.*[42] for non-polarizable systems and the density-readjusting embedded atom model (DR-EAM) by Bhattarai *et al.*[38] for polarizable systems. These two models give nearly identical bulk metallic properties for gold, but differ in how they interact with charged and polar species at the surface of the metal. All systems were solvated in liquid water which was simulated using the SPC/E water model.[43] Water molecules were simulated as rigid bodies, so no bond or angle constraints were imposed.

The thiolated PEG parameters were adapted from multiple sources. The TraPPE united-atom force field was utilized for most Lennard-Jones parameters, bond lengths, and bend and torsion parameters.[44–46] We implemented a fully flexible thiolated PEG model, and bond stretch force constants were adapted from OPLS-UA and OPLS-AA.[47,48] The cross interactions between gold and other atom types were adapted from Schapotschnikow *et al.*[49]

Interactions between gold and water were modified from the Mie potential from Dou *et al.*[50] The details of all force field parameters are provided in the Supporting Information (SI).

Simulation Protocol

The following systems of interest were constructed: Planar interfaces of single-crystalline gold exposing the (111), (110), and (100) facets, as well as spherical gold nanoparticles (10 Å and 20 Å radii). These five systems were studied using both non-polarizable (EAM) and polarizable (DR-EAM) metallic models, yielding a total of ten unique systems. All metallic systems were constructed with a lattice constant of 4.08 Å. For each system, four statistically independent samples were created by resampling the positions of the thiolated PEG molecules at the gold surfaces using Packmol.[51] In all systems, the sulfur atoms of the thiolated PEG molecules were initially placed within 3 Å of the gold surface. Orientational preferences were enforced in the initial configurations by placing the terminal hydroxyl hydrogen at least 9 Å away from the same surface. On nanoparticles (centered at the origin), the sulfur atoms were placed inside a sphere that was 1-3 Å larger than the radius of the nanosphere, while orientations enforced by placing hydroxyl hydrogens at least 10 Å farther away from the nanoparticle surface. These yielded relatively uniform initial orientations for all ligand molecules. Built-in OpenMD utilities were used to combine the metal and ligand components and to solvate the systems. Each system then underwent steepest descent structural optimization prior to equilibration.

Initial atomic velocities were sampled from a Maxwell-Boltzmann distribution at 300 K. Planar systems then underwent structural relaxation for 20 ps in the canonical (NVT) ensemble, followed by a 400 ps equilibration in an isobaric-isothermal (NPT) ensemble with characteristic time constants, $\tau_{\text{barostat}} = 5000$ fs and $\tau_{\text{thermostat}} = 100$ fs to adjust the volume of the simulation cell. This was followed by 200 ps of thermal equilibration (NVT) with $\tau_{\text{thermostat}} = 100$ fs and 200 ps of equilibration in the microcanonical (NVE) ensemble. These systems were subsequently simulated for 100 ps in the NPAT (constant normal pressure with the surface area of the interface held constant) ensemble. A Nosé-Hoover thermostat[52] and modified Nosé-Hoover-Andersen[53] barostat were used for constant temperature and pressure ensembles, respectively. A time step of 1 fs was used for all simulations.

Spherical gold nanoparticles were constructed by carving out a spherical region from an fcc lattice ($a = 4.08$ Å) with a radius of either 10 or 20 Å. The atoms were assigned velocities from a Maxwell-Boltzmann distribution at 5 K, and the pristine nanoparticles were incrementally equilibrated at 5 K, 100 K, 200 K, and lastly 300 K in a Langevin Hull,[54] which can sample constant temperature and pressure ensembles in non-periodic systems. As described above, Packmol and OpenMD were used to resample ligand positions and combine components.[51,55] One gold atom closest to the origin in each nanoparticle was given an artificially large mass to prevent the nanoparticle from drifting. These non-periodic systems were first equilibrated for 200 ps using the Langevin Hull integrator[54] and a resampling of velocities from a Maxwell-Boltzmann distribution at 300 K every ps. This was followed by an additional 250 ps of equilibration using the Langevin Hull integrator without velocity resampling.

All systems were built with similar thiolated PEG surface densities (4.70 molecules/nm^2 for spherical systems with a gold radius of 10 Å, 4.66 molecules/nm^2 for spherical systems with a gold radius of 20 Å, 4.81 molecules/nm^2 for planar (111) facets, 4.67 molecules/nm^2 for planar (110) facets, and 4.63 molecules/nm^2 for planar (100) facets. These densities amount to an approximate coverage of 1 thiolated PEG molecule for every 3 surface gold atoms. Representative configurations of the systems are shown in Figure 1.

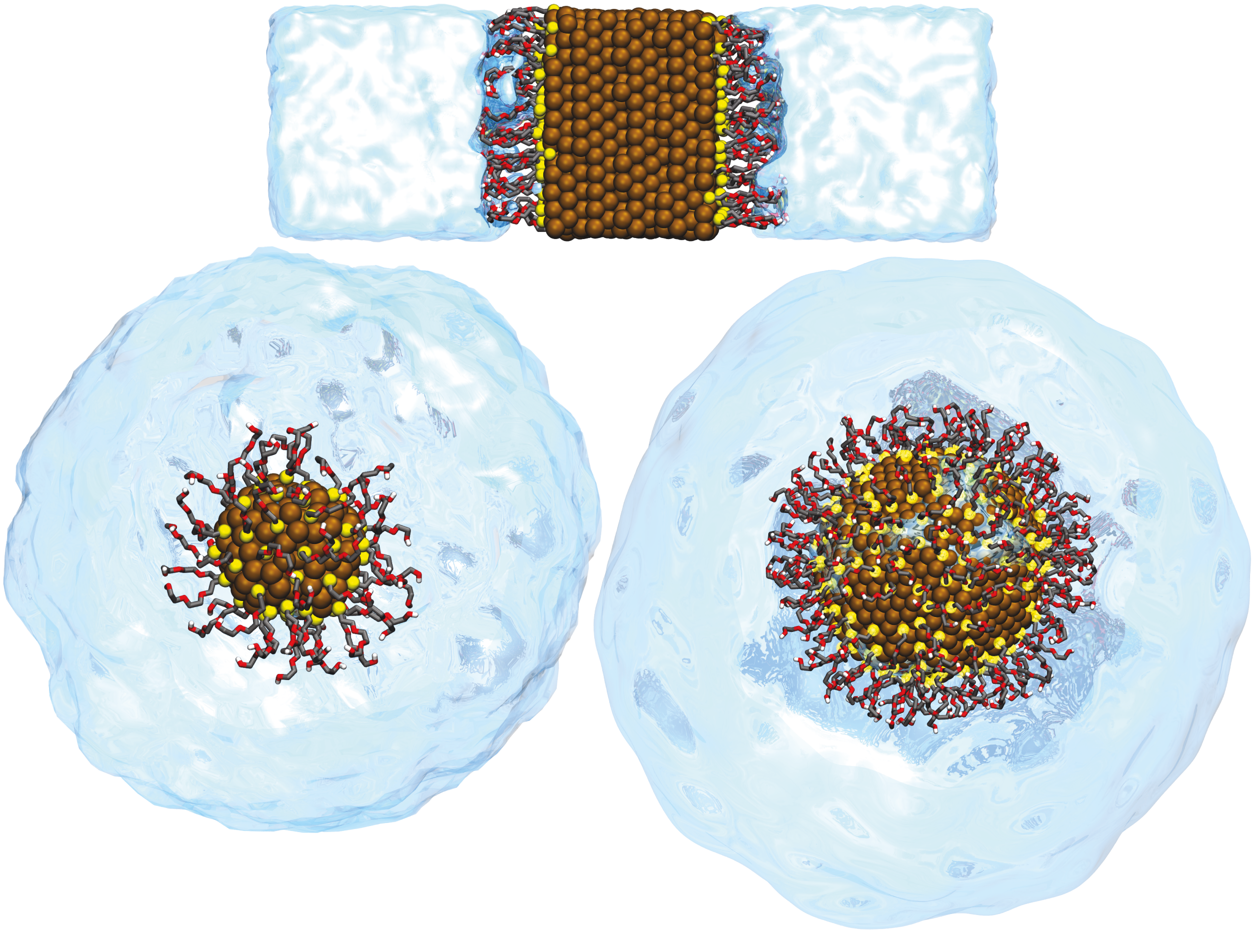

Figure 1: Representative configurations of the simulated systems. Top: Au(111) facet functionalized with thiolated PEG and solvated in SPC/E water. Bottom left: A gold nanosphere with a 10 Å radius. Bottom right: A gold nanosphere with a 20 Å radius. Gold and sulfur atoms have been represented with van der Waals spheres. The rest of the united atom thiolated PEG ligands are shown with bonds. The SPC/E water occupies the remaining volume. Detailed specifications of these systems are provided in the Supporting Information (SI).

After equilibration, a thermal flux was applied to all systems using the velocity shearing and scaling (VSS) RNEMD methodology developed by Kuang and Gezelter.[41] The magnitude of the thermal flux was chosen so that the heat rate through the metal/solvent interface was approximately equal in all systems. The applied thermal flux was 8.8×10^{-6} kcal mol^{-1}Å^{-2} fs^{-1} (6100 MWm^{-2}) for nanoparticles with a radius of 10 Å, 3.6×10^{-6} kcal mol^{-1}Å^{-2} fs^{-1} (2500 MWm^{-2}) for the 20-Å nanoparticles, and 5.0×10^{-6} kcal mol^{-1}Å^{-2} fs^{-1} (3500 MWm^{-2}) for all planar systems. The thermal flux was applied for 5 ns in all systems.

Calculation of Thermal Transport Properties

To calculate the thermal conductivity (λ) in the bulk solvent phase, we can use Fourier's law,

$$\mathbf{J} = -\lambda \nabla T, \tag{3}$$

where $\mathbf{J}$ is the thermal flux and ∇T is the temperature gradient. In RNEMD simulations, $\mathbf{J}$ is an (unphysical) applied perturbation, and the system responds by creating a thermal gradient. In planar systems, the thermal flux is applied in a direction normal to the interface (in this case the z-axis). From the applied flux, J_z, we can also calculate the interfacial thermal conductance,

$$G = \left(\frac{J_z}{\Delta T} \right) \tag{4}$$

where ΔT is the temperature difference calculated across the interface.

In planar systems, thermal gradients are computed using histograms containing local information about the temperature in 1.8 Å wide bins which span the width and breadth of the system. We define the interfacial region, i.e. the region spanning the metal / ligand / solvent interface, from the last bin which contains only gold atoms to the first bin which contains only water. In computing the interfacial thermal conductance, the temperature jump, ΔT, is measured across the entire interfacial region. Calculations of solution-phase thermal conductivity (λ) include only bins in the pure solvent phase.

For spherical nanoparticles, we use a series approximation for the Kapitza resistance for concentric spherical shells,

$$R_K = \frac{1}{G} = \frac{1}{q_r}\sum_i 4\pi r_i^2 \left(T(r_{i+1}) - T(r_i)\right) \tag{5}$$

The idea here is that heat must pass through successive spherical shells with an identical radial heat rate, q_r, rather than the applied radial flux, J_r. We accumulate statistics on 1.25 Å wide shells, but here each shell has a different surface area and volume. Shell i has inner radius r_i, and the average temperature of that shell is $T(r_i)$. The interfacial region is defined as a finite-width region starting at a shell containing only gold atoms and ending at a shell containing only water. In previous work, we showed that varying the width of the interface used for calculating G remains relatively stable as long as it spans the entire interfacial region.[40] Transfer of heat from one shell to another contributes a small amount to the Kapitza resistance. The total resistance for the interface is therefore the sum of all concentric contributions, yielding the finite width approximation for the interfacial thermal conductance in Eq. (5).

Results and Discussion

Thermal Transport Properties

The solvent thermal conductivity and interfacial thermal conductance values for planar interfaces are shown in Table 1. As expected, solvent thermal conductivity values are similar to those calculated in pristine Au(111). However, the values of G are higher here compared to the pristine interface.[40] In this work, there is no significant difference in G across the planar facets in contact with the ligand, meaning that the surface ordering of gold atoms does not dominate thermal transport in these systems.

The interfacial thermal conductance values for spherical systems are shown in Table 2. Com-

Table 1: Solvent Thermal Conductivity (λ) and Interfacial Thermal Conductance (G) Values for Systems Containing Planar Gold Interfaces Capped with Thiolated PEG

Facet	Metal	λ ($\mathrm{Wm^{-1}\,K^{-1}}$)	G ($\mathrm{MW\,m^{-2}\,K^{-1}}$)
(111)	non-polarizable	1.02 ± 0.02	211 ± 15
	polarizable	1.01 ± 0.03	208 ± 4
(110)	non-polarizable	1.01 ± 0.03	215 ± 7
	polarizable	1.01 ± 0.03	217 ± 8
(100)	non-polarizable	0.98 ± 0.04	207 ± 9
	polarizable	1.00 ± 0.03	209 ± 5

pared with the planar interfaces, the reported mean values of G are larger for systems with higher curvature, but we note that only a few of these values fall outside of the 95% confidence intervals of comparable systems, i.e. the same treatment of metal polarizability. The differences in the value of G for 10 Å and 20 Å particles fall within confidence intervals.

Table 2: Interfacial Thermal Conductance (G) Values for Systems Containing Spherical Gold Interfaces Capped with Thiolated PEG

Radius	Metal	G ($\mathrm{MW\,m^{-2}\,K^{-1}}$)
10 Å	non-polarizable	250 ± 25
	polarizable	217 ± 77
20 Å	non-polarizable	307 ± 112
	polarizable	244 ± 45

To examine the organization of the ligand and solvent layers, we have computed the thermal profiles and local mass densities of each species in the systems of interest. These are shown in Figure 2 (and for the polarizable surface in the Supporting Information). We note that the temperature drops most sharply between the gold surface and the sulfur atoms on the ligand, indicating location of highest thermal resistance ($R_K = 1/G$). While ballistic transport can occur across molecular junctions,[37] there is a significant amount of disorder present at this interface. As can be seen in the mass density profiles, the thiolated PEG molecules partially penetrate the first surface gold layer, embedding sulfur atoms in the top gold plane, and displacing a few surface gold atoms. This penetration occurs to the greatest extent at the Au(111) interfaces. The water molecules also display less ordered layering directly adjacent to the bound ligands in these systems, suggesting that the embedding behavior of the thiolated PEG directly affects the structuring of the solvent. We also note an appreciable density of water that congregates in the spaces between the thiolated PEG molecules. Other than slight differences in thiolated PEG penetration at Au(111) interfaces, metal polarizability appears to make no significant difference in the ordering and structure of any species. Thermal profiles and mass densities of each species in planar systems using the polarizable DR-EAM metallic potential are available in the SI.

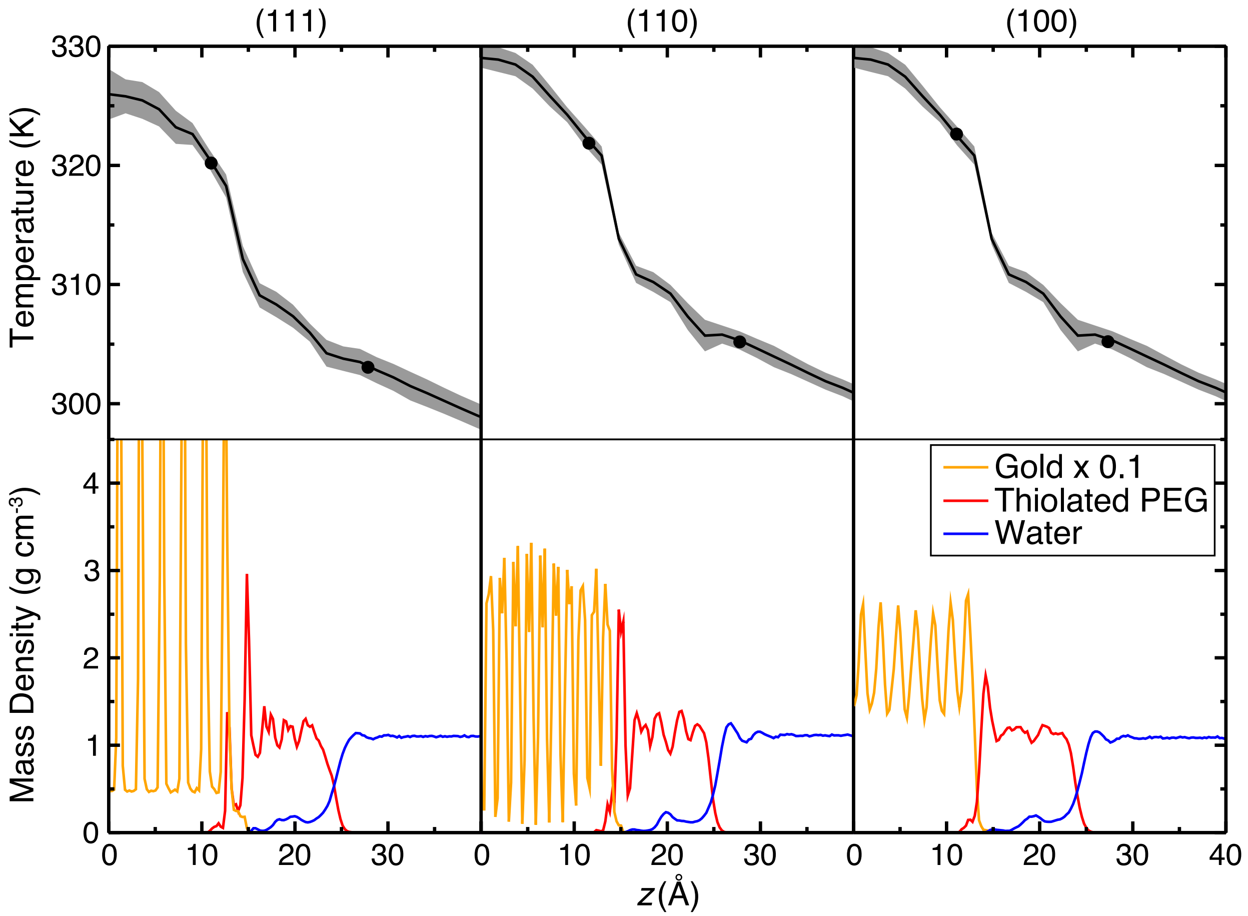

Figure 2: Under an applied thermal flux, temperature drops are largest at the location of the Gold-Sulfur bond. (Top) Thermal profiles of planar systems simulated using the non-polarizable EAM potential. Shading indicates the 95% confidence interval for computed temperatures, while the black dots are the bounds of the interfacial region used for computing conductance. (Bottom) Mass densities of each species. $z = 0$ represents the center of the gold slabs.

The thermal profiles and local mass densities of all species in the non-polarizable nanosphere systems are shown in Figure 3. Note that in the nanoparticle systems, average solvent temperatures at the Langevin Hull (far from the particle) spanned a range from 288-301 K, so we show here the temperature difference from the solvent near the hull, *i.e.*, as $r \to \infty$. When plotted this way, temperature gaps at the interface are relatively uniform across different samples. The water shows more embedding in the thiolated PEG layer than in planar systems, and more embedding of the ligand layer is also apparent. As in the planar systems, the thiolated PEG partially penetrates into the surface of the gold nanospheres. One notable feature is that the water appears to be clustered near the oxygen atoms in the thiolated PEG layer, suggesting that local hydrogen bonding may be important. The thermal profiles and local mass densities for the polarizable nanosphere systems are available in the SI, as metal polarizability appears to make no difference in the mass density picture, and there are no obvious particle radius effects that would influence the amount of contact between any species.

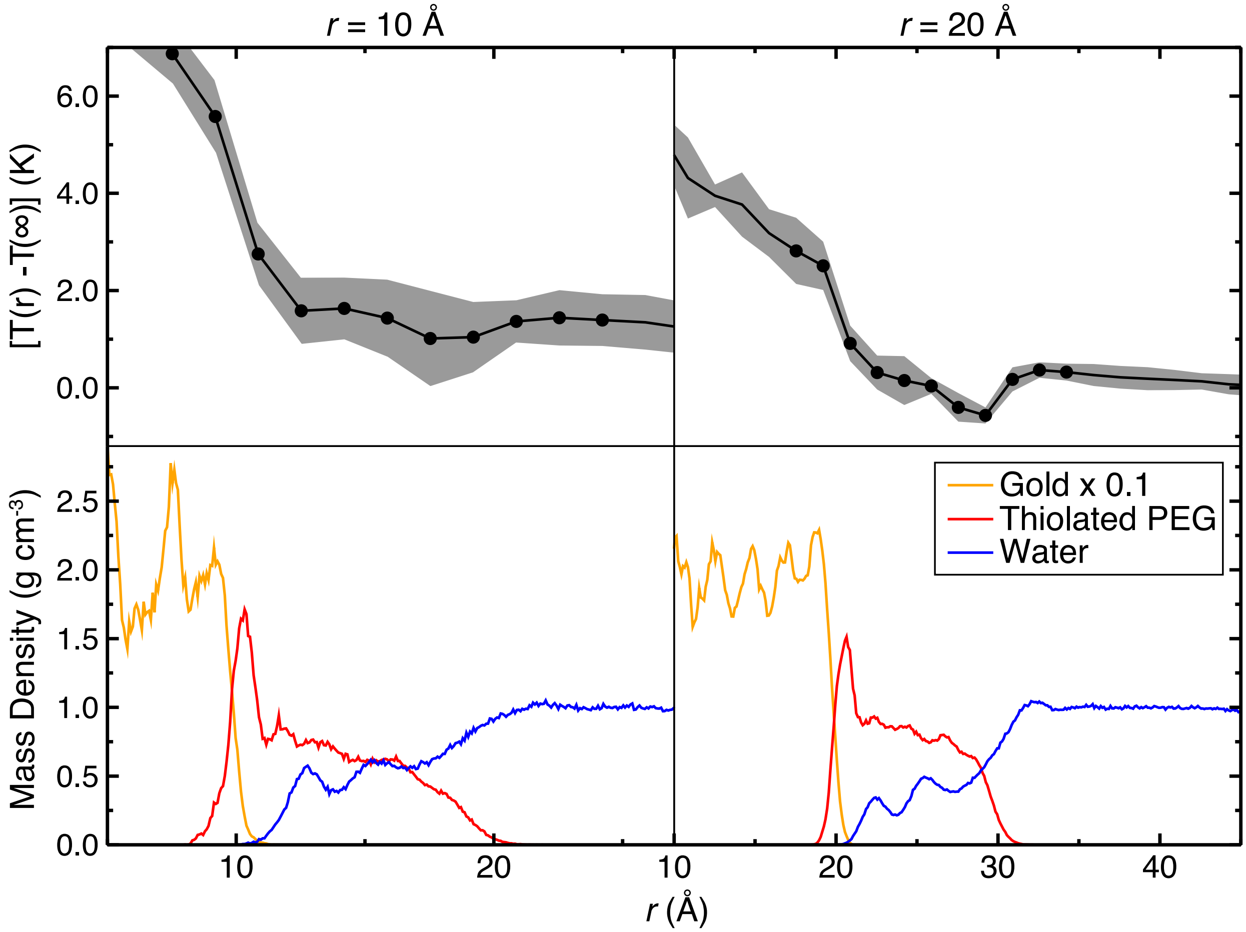

Figure 3: In the nanospheres, temperature drops under an applied thermal flux are also largest at the Gold-Sulfur bond. (Top) Thermal profiles of nanoparticle systems, relative to the temperature of the solvent far from the particle. The shaded region represents the 95% confidence intervals. The black data points are the temperature differences in the Kapitza region which were used for calculating conductance. (Bottom) Local mass densities of each species for the nanoparticles using the non-polarizable EAM model. $r = 0$ is at the center of the gold nanosphere.

The large observed interfacial thermal conductance in these systems would require coupling between both the metal surface and the ligand, and between the ligand and solvent. The strong Au-S bonding interaction provides the metal-to-ligand coupling, but what provides ligand-to-solvent coupling? Other groups have commented on the potential link between increased solvent-ligand interactions and an increase in G.[24–26,30] To quantify the physical overlap between species, we explored whether molecules in the same physical region (i.e. the ligand layer) had probability of being at the same physical distance from the interface. We calculated the Bhattacharyya coefficient (BC) for each pair of species using normalized mass densities to determine probability densities. In planar systems containing molecules A and B,

$$BC = \int_{z_L}^{z_R} \sqrt{p_A(z) p_B(z)}\, dz \tag{6}$$

where $p_A(z)$ and $p_B(z)$ are the probability densities of molecules A and B, respectively, calculated using

$$p_A(z) = \frac{\rho_A(z)}{\int_{z_L}^{z_R} \rho_A(z)\, dz} \tag{7}$$

for species A, where $\rho_A(z)$ is the mass density of species A and the bounds of the integrals are the outermost locations of the thiolated PEG in the z direction. Similarly, for spherical systems,

$$BC = \int_{r_{\text{inner}}}^{r_{\text{outer}}} 4\pi r^2 \sqrt{p_A(r) p_B(r)} dr \tag{8}$$

where $p_A(r)$ and $p_B(r)$ are the probability densities of molecules A and B, respectively. Likewise, in spherical geometries, the probability densities,

$$p_A(r) = \frac{\rho_A(r)}{\int_{r_{\text{inner}}}^{r_{\text{outer}}} 4\pi r^2 \rho_A(r) dr} \tag{9}$$

for species A, where $\rho_A(r)$ is the mass density for molecule A and the bounds of the integrals span all values r containing thiolated PEG. The resulting BC values are unitless numbers between 0 and 1, where 0 signifies no overlap between the two species and 1 signifies complete overlap in the ligand region. A higher BC would indicate increased contact between two species. We note that in other investigations of thermal transport at metal / non-metal interfaces, Bhattacharyya coefficients have been calculated using the vibrational densities of states (VDOS) of two species at an interface,[34] while the treatment here provides a measure of physical interpenetration rather than vibrational overlap. However, we have also investigated the vibrational overlap, which is shown in Table S10 in the SI.

To investigate the extent of contact between the two pairs of molecules, we calculated the corresponding BC values which are shown in Table 3. There is a large amount of overlap between water and thiolated PEG, with little difference across the three planar geometries. Additionally, gold polarizability does not significantly alter the BC in either the planar or spherical cases. Interestingly, the BC values in the spherical systems are higher than those for the planar systems, indicating significantly more physical contact between the ligand and solvent. This could explain a mechanism for enhanced thermal transport at curved nanoparticle interfaces (relative to their planar counterparts) with porous ligand layers.

In the planar systems, the density-based BC values confirm that the (111) facet has more embedding of the thiolated PEG into the top gold layer (see Figure 2). However, the difference in BC values here is small. Water / thiolated PEG BC values indicate nearly identical overlap across all facets, and this is reflected in the resulting values of G.

Factors Governing Ligand-to-Solvent Coupling

The strong metal-to-ligand coupling is one reason that G is relatively high in these systems, but the orientation, interpenetration, and hydrogen bonding preferences of the thiolated PEG molecules are all worth investigating, as previous work has correlated ligand-to-solvent orientational alignment with increased thermal transport.[25] We determined the average alignment of ligand molecules relative to the gold surface by calculating the second order Legendre parameter,

$$\langle P_2 \rangle = \frac{1}{2} \left\langle 3\cos^2\theta - 1 \right\rangle \tag{10}$$

Table 3: Bhattacharyya Coefficients showing degree of density overlap between the thiolated PEG and the other two components of the metal / ligand / water systems.

Facet	Metal	BC with thiolated PEG (unitless)	
		Water	Gold
(111)	non-polarizable	0.552 ± 0.028	0.107 ± 0.032
	polarizable	0.526 ± 0.034	0.126 ± 0.026
(110)	non-polarizable	0.564 ± 0.025	0.048 ± 0.011
	polarizable	0.557 ± 0.038	0.050 ± 0.005
(100)	non-polarizable	0.559 ± 0.059	0.058 ± 0.012
	polarizable	0.554 ± 0.043	0.043 ± 0.008
NP ($r = 10$ Å)	non-polarizable	0.671 ± 0.038	0.258 ± 0.037
	polarizable	0.661 ± 0.023	0.302 ± 0.031
NP ($r = 20$ Å)	non-polarizable	0.664 ± 0.029	0.201 ± 0.052
	polarizable	0.684 ± 0.026	0.175 ± 0.095

where θ is the angle between the vector between the sulfur and terminal hydroxyl hydrogen atoms in each thiolated PEG molecule and the vector normal to the metal surface at the attachment point. If all thiolated PEG molecules are oriented perpendicular to the metal surface, then $\langle P_2 \rangle = 1$. Likewise, completely disordered ligands will produce $\langle P_2 \rangle = 0$.

The orientational order parameters for all systems are shown in Table 4. Within confidence intervals, the planar interfaces exhibit ligand chain ordering that are independent of facet, while high curvature nanospheres ($r = 10$ Å) show the lowest orientational ordering. The lower curvature nanospheres ($r = 20$ Å) are intermediate. We note that there is a slight preference for ligand ordering on the (110) facet relative to the other planar facets. Most of the orientational ordering parameters for non-polarizable planar systems are within error of their polarizable counterparts. There is a significant increase in ligand ordering in the larger nanospheres when the gold is polarizable, although this is the only system that exhibits this behavior. The lower orientational ordering

Table 4: Structural properties of the planar and nanosphere interfaces. This table provides second order Legendre parameters and Hydrogen bond surface densities.

Gold Structure	Metal	$\langle P_2 \rangle$ (unitless)	H-bonding density (Å^{-2})
(111)	non-polarizable	0.819 ± 0.013	0.147 ± 0.002
	polarizable	0.819 ± 0.007	0.147 ± 0.007
(110)	non-polarizable	0.836 ± 0.013	0.142 ± 0.003
	polarizable	0.835 ± 0.014	0.145 ± 0.005
(100)	non-polarizable	0.805 ± 0.009	0.144 ± 0.002
	polarizable	0.812 ± 0.014	0.143 ± 0.005
NP (r = 10 Å)	non-polarizable	0.709 ± 0.010	0.132 ± 0.002
	polarizable	0.715 ± 0.006	0.131 ± 0.001
NP (r = 20 Å)	non-polarizable	0.743 ± 0.006	0.116 ± 0.002
	polarizable	0.759 ± 0.006	0.118 ± 0.002

in the nanosphere systems is to be expected, as the configurational volume available to the terminal ends of the chains is significantly higher than in the planar systems (with the same surface packing density).

To further probe the ligand-solvent interactions, we determined the hydrogen bonding density between water and thiolated PEG. We examined all potential donor and acceptor atoms (including the hydroxyl hydrogen) inside hydrogen bonding distance (3.5 Å) from water, with an HOH angle cutoff of 30°. Local hydrogen bond densities were computed as a function of surface normal coordinate (z in the planar systems, r in the nanospheres). Hydrogen bond densities and ligand mass densities are shown in Figure 4, and the integrated hydrogen bond densities are shown in Table 4. These values provide a density of ligand-to-solvent hydrogen bonds per surface area of the metal. For planar systems,

$$\text{H-bonding density per Å}^2 = \int_0^z \rho(z)dz \tag{11}$$

where $\rho(z)$ is the hydrogen bonding per Å^3. For spherical systems, integration is done in spherical coordinates,

$$\text{H-bonding density per Å}^2 = \int_0^\infty \left(\frac{r}{R}\right)^2 \rho(r)dr \tag{12}$$

where $\rho(r)$ is the hydrogen bonding per Å^3 and R is the radius of the gold nanosphere.

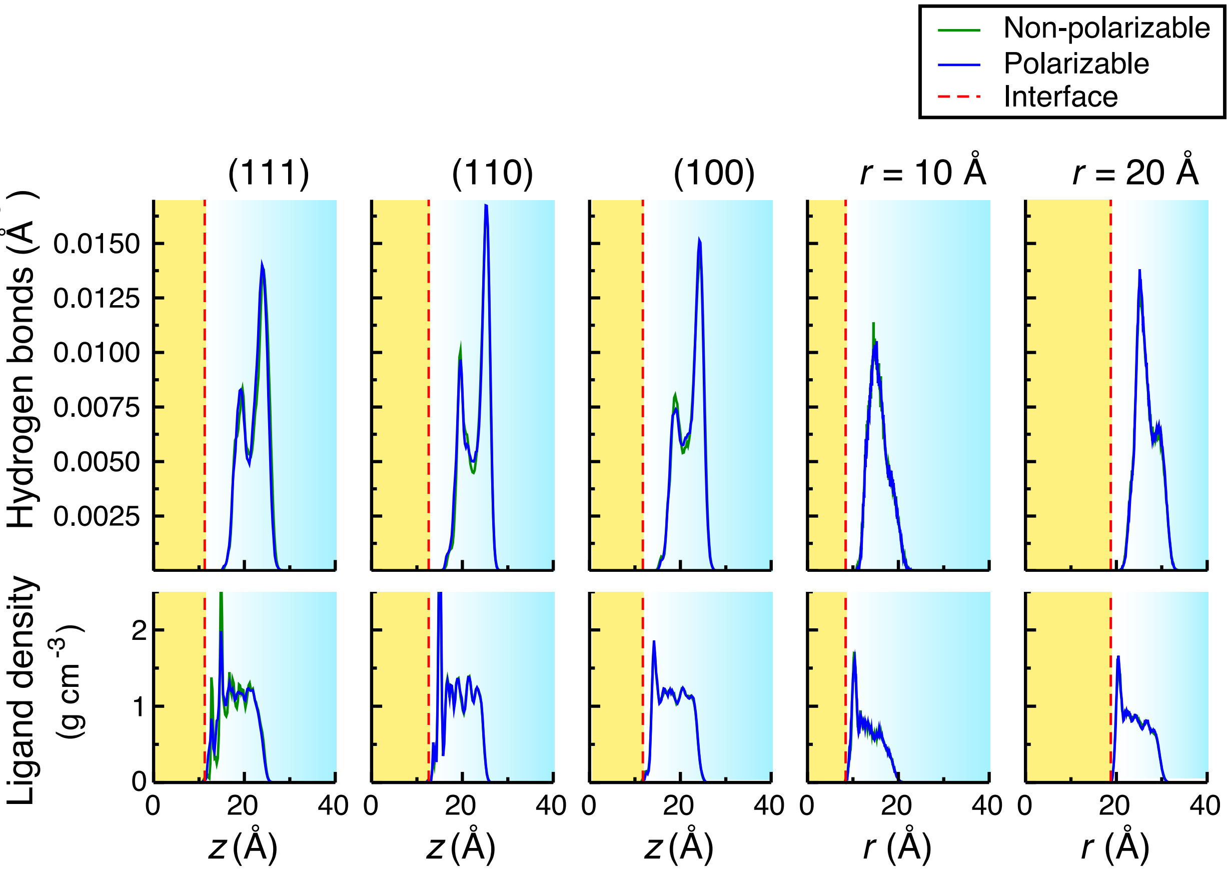

Figure 4: Hydrogen bonding densities (Top) and ligand mass densities (Bottom) for all interfaces, illustrating the changes in the network of hydrogen bonding between planar and nanoparticle systems. Metal polarizability does not significantly change the hydrogen bonding densities, while the shape and size of the gold particle appear to have an impact. The planar systems exhibit the most hydrogen bonding involving the terminal oxygen, while hydrogen bonding with an ether oxygen is most prevalent in the nanospheres. Gold surface curvature affects the configurational freedom in thiolated PEG chains, and determines how many water molecules can come within hydrogen bonding distance of the ligand.

From this data, we can determine which atoms in the thiolated PEG ligand are responsible for hydrogen bonding, and how the magnitude of hydrogen bonding varies as a function of metal polarizability, facet, shape, and size. An extensive hydrogen bonding network between thiolated PEG and water would mean an additional layer of contact between the ligand and solvent, possibly explaining the high *G* values.

In Figure 4, the planar systems each display two distinct peaks, where each peak represents hydrogen bonding at one of the oxygen atoms in the ligand. The outermost peak comes from the terminal hydroxyl group. The other, based largely on spacing between the peaks, is due to an ether oxygen that is three atoms closer to the surface, while the oxygen closest to sulfur does not participate in hydrogen bonding. In the planar systems, the majority of hydrogen bonding is occurring at the terminal oxygen. Due to the densely packed network of thiolated PEG molecules, fewer water molecules are able to congregate between them to facilitate hydrogen bonding. The magnitude of the hydrogen bonding densities are similar across all planar geometries.

For spherical systems, hydrogen bonding with water favors one of the ether oxygen atoms, although the terminal hydroxyl group also participates. As in the planar systems, the ether oxygen most likely to form hydrogen bonds is the outermost one. It is also useful to note that the total hydrogen bonding per unit area of the gold surface is reduced in the nanospheres (see Table 4). We observe a higher degree of ligand-to-water hydrogen bonds in the planar system, but the hydrogen bonding is deeper in to the ligand layer for the nanospheres. Polarizability does not appear to significantly affect the magnitude or distribution of hydrogen bonding for any system.

Additionally, we computed charge densities as a function of distance from the interfaces. Although there are some observable differences between facets and between the planar systems and the nanospheres, particularly on the thiolated PEG side of the interface, the polarizability model appears to have little effect on the interfacial thermal conductance in these systems. Plots of charge densities are provided in the SI.

Analysis of Vibrational Power Spectra

The models most widely used to understand interfacial thermal transport have their origins in the diffuse mismatch model (DMM).[56] Although it is rarely quantitative and does not consider interactions between adjoining materials, the DMM can point to factors responsible for enhanced (or diminished) heat transfer. It assumes that phonons that strike the interface are elastically scattered and transferred into the adjoining material with a transmission probability that depends on the phonon densities of states (DOS) in the two materials. At the interface between materials *a* and *b*, the interfacial thermal conductance,

$$G_{ab} = \frac{1}{4\pi}\sum_{p}\int_{0}^{\pi/2}\sin\theta d\theta\int_{0}^{2\pi}d\phi\int_{0}^{\infty}d\omega\,\left(\hbar\omega\frac{\partial f}{\partial T}v_a\rho_a(\omega)\tau_{ab}\cos\theta\right) \tag{13}$$

where f is the Bose-Einstein function,

$$f(\omega,T) = \frac{1}{\left(e^{\hbar\omega/k_BT}-1\right)}, \tag{14}$$

and phonons with a polarization p, group velocity $v_a(\omega,p)$, and incident angles θ and ϕ are transmitted between a and b with a transmission probability $\tau_{ab}(\omega)$.[57]

If we assume that the transmission probability and group velocity do not depend on incident scattering angle, the angular integrals are easily solved. Additionally, the derivative of the Bose-Einstein function has the effect of weighting the lowest frequency portion of the vibrational densities of states. One of the simplest models for the transmission probability involves using detailed balance to connect forward and reverse scattering at a frequency ω, that is, $\tau_{ab}(\omega) = 1-\tau_{ba}(\omega)$. The connection between G_{ab} and G_{ba} is made clear by treating the remaining contribution to interfacial thermal conductance in a symmetric form,

$$\rho_a(\omega)\tau_{ab}(\omega) \approx \frac{\rho_a(\omega)\rho_b(\omega)}{\rho_a(\omega)+\rho_b(\omega)}. \tag{15}$$

This shows the importance of having the same phonon frequencies present on both sides of the interface in order to carry heat between a and b (and between b and a). This portion of the integrand only survives if both materials have contributions at the same frequencies. We note that while the DMM has limited success as a predictive theory, we can still use it to interpret features in our vibrational power spectra that may explain the higher mean G values in the nanospheres.

To explore the roles of particle curvature, internal hydrogen bonding and metal polarizability, we have computed the power spectra for vibrational motion,

$$\rho(\omega) = \frac{1}{\sqrt{2\pi}} \int_{-\infty}^{\infty} \langle \mathbf{v}(t) \cdot \mathbf{v}(0) \rangle e^{-i\omega t}\, dt \tag{16}$$

where the angle bracket averages over all particles of a given type. We divided the systems into four regions, interfacial gold (within 5 Å of the interface), the ligand itself, interfacial solvent that is embedded in the thiolated PEG layer, and bulk solvent that lies outside of the ligand layer, for both the planar and nanoparticle systems. Each system was simulated for an additional 50 ps in the NVE ensemble for the planar systems and the Langevin Hull for the nanoparticle systems. Velocity autocorrelation functions with a time granularity of 3 fs were calculated from these trajectories. The power spectra are discrete Fourier transforms of these autocorrelation functions. Power spectra were normalized so that they integrate to unity over the entire frequency range.

We find that the power spectra do not depend on the polarizability model used to represent the metal, and we also observe very similar spectra for all three planar metal facets. Similarly, the power spectra for the two nanosphere systems are nearly identical. To aid in comparison, we have computed the spectra, averaged across metal facet (for the planar systems) and polarizability. For spherical systems, the spectra were averaged for particles of different radii and polarizability. For completeness, the spectra for all components of the individual systems can be found in the SI (Figures S5 and S6).

The averaged power spectra for the gold, thiolated PEG, and the interfacial solvent are shown in Figure 5. In the gold nanospheres, we observe a broadening and shift in the higher frequency peak that has been previously attributed to undercoordinated gold atoms at the surfaces of the spheres.[31,32] We also observe an increase in the low frequency heat carrying modes (0 - 70 cm^{-1}) for the thiolated PEG. Because of the Bose-Einstein weighting of lower frequency modes, the enhanced population at these frequencies may explain the higher mean G values found in the nanospheres. In the interfacial solvent, there is again an increased population at low frequencies for the spherical systems, here between 0 - 80 cm^{-1}. We also note the lack of overlap between the thiolated PEG and gold spectra at low frequencies which potentially explains the larger temperature drop between the two species.

We have also tabulated the Bhattacharyya coefficients (BC) from vibrational power spectra for the same pairs of species as in Table 3, which are available in the SI. Here, the integral range spans all computed frequencies (0 - 6000 cm^{-1}). While the mean BC value for the gold / thiolated PEG pair is higher in the 10 Å nanospheres, the overlap between all other pairs is nearly the same for all systems, likely due to the unbiased frequency weighting in the calculation of these coefficients.

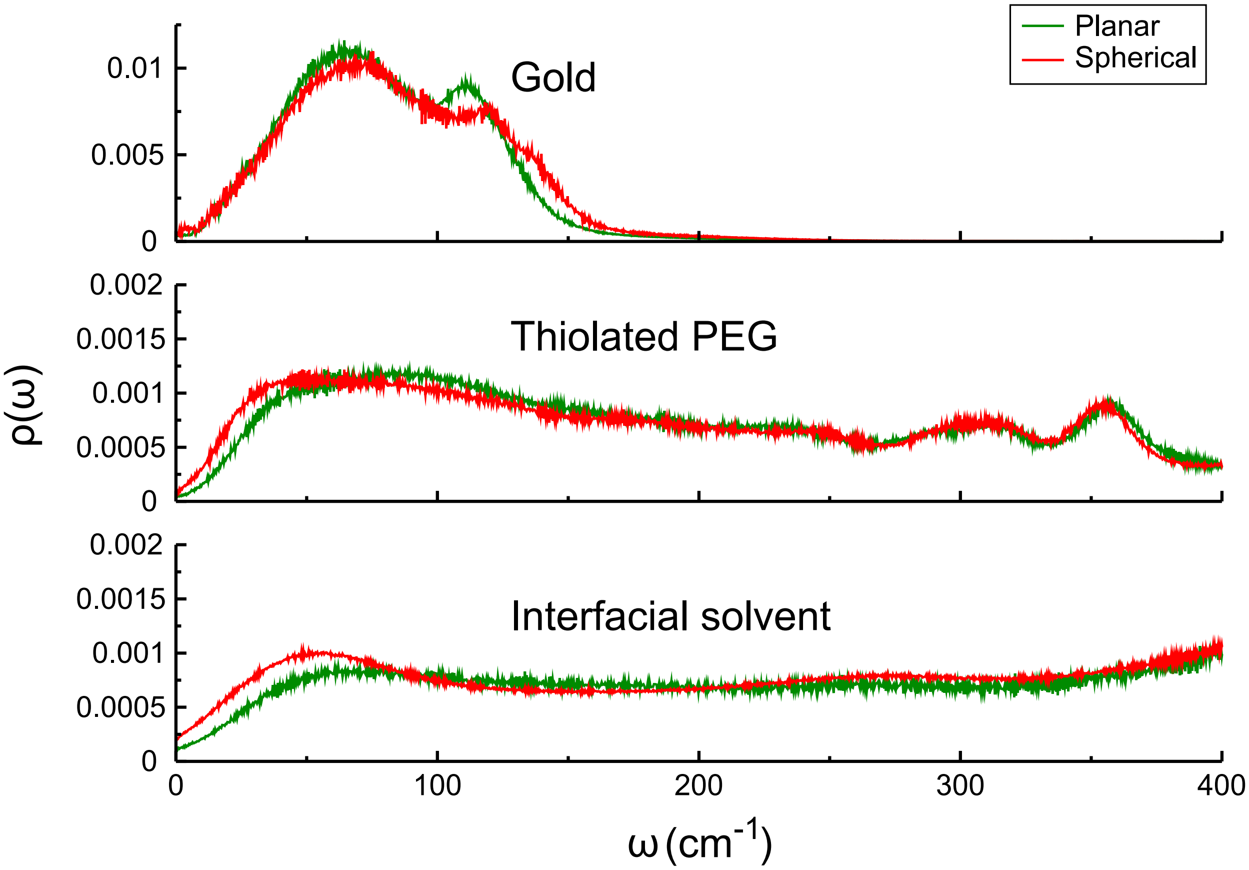

Figure 5: Averaged power spectra for gold, thiolated PEG and the interfacial solvent in planar and nanosphere systems. We show here only the moderate frequency portion ($0 - 400\ \mathrm{cm}^{-1}$). Lower-frequency modes attributed to collective motion are most important for heat transfer, and we observe a slightly higher population from $0 - 80\ \mathrm{cm}^{-1}$ in the interfacial layers attached to the nanospheres. This difference persists into the interfacial solvent that is trapped in the thiolated PEG layer. Note that the planar curve is an average of all polarizable and non-polarizable simulations of (111), (110), and (100) facets, and the spherical curve is an average of all polarizable and non-polarizable simulations of nanospheres with radii of 10 and 20 Å.

Conclusions

We have studied the effects of metal polarizability, shape, facet, and size on heat transfer processes in gold interfaces functionalized with a low molecular weight thiolated PEG. We found that the mean values of G in spherical systems are generally higher than those in planar systems. We have also determined that metal polarizability and the choice of planar facet make little difference in heat transfer processes in these systems. Additionally, the solvent thermal conductivity remains nearly constant for all planar systems with the same ligand grafting density. From thermal profiles, we determined that the largest temperature drop occurs between the gold surface and sulfur atoms in thiolated PEG, meaning that thermal resistivity is highest at this portion of the interface.

We observed overlap in the mass densities of thiolated PEG and gold, meaning that the ligands are capable of penetrating and disrupting the gold surface. From the corresponding Bhattacharyya coefficients, we determined that there is an increased amount of physical contact between all adjacent pairs of species in the nanospheres. We also found that there is an enhanced population of low frequency heat-carrying modes in the vibrational power spectra of the thiolated PEG and interfacial solvent in the nanospheres, and this may contribute to the higher mean G values in those systems. The thiolated PEG molecules are less ordered in the spherical systems, with a larger configurational volume available for the terminal ends of the ligands. The ether oxygen in thiolated PEG participates in hydrogen bonding with the solvent to a greater degree than the terminal hydroxyl group here, a trend that is reversed in planar systems. Interestingly, there is an overall lower hydrogen bonding density in the nanospheres than in planar systems. Our results suggest that the strong metal-to-ligand coupling present in thiolated PEG on gold is important for interfacial thermal conductance. This appears to dominate the effects of metal polarizability, facet, and surface curvature. There may be also be a weak dependence on the location and kind of ligand-to-solvent hydrogen bonding.

Thiolated PEG is a biocompatible non-ionic ligand which allows gold nanoparticles to be solvated in water. It may not be a surprise that metal polarizability is relatively unimportant for interfacial thermal conductance through a non-ionic protecting group, but there are other bio-compatible, aqueous, *ionic* ligands, such as cetyltrimethylammonium bromide (CTAB), which are candidates for protecting nanospheres in photothermal therapies. CTAB also has a different binding affinity to gold than thiolated PEG, and it prevents gold aggregation through a different mechanism (i.e., through the formation of micelles). Studies of other biocompatible ligands would help us better understand how heat transfer is affected by the same factors studied here, as well as how the ionic character of such a ligand would affect interfacial thermal conductance.

Acknowledgement

Support for this project was provided by the National Science Foundation under grant CHE-1954648. Computational time was provided by the Center for Research Computing (CRC) at the University of Notre Dame. The authors would also like to thank Benjamin M. Harless and C.R. Drisko for helpful discussions regarding data analysis.

Supporting Information Available

Details regarding system composition, force field parameters, equilibration, method validation, data collection, additional vibrational power spectra, thermal profiles, mass densities, and charge densities described in this work.

References

(1) Vines, J. B.; Yoon, J.-H.; Ryu, N.-E.; Lim, D.-J.; Park, H. Gold Nanoparticles for Photothermal Cancer Therapy. *Front. Chem.* **2019**, *7*, 1–16.

(2) Huang, X.; El-Sayed, M. A. Gold nanoparticles: Optical properties and implementations in cancer diagnosis and photothermal therapy. *J. Adv. Res.* **2010**, *1*, 13–28.

(3) Bai, X.; Wang, Y.; Song, Z.; Feng, Y.; Chen, Y.; Zhang, D.; Feng, L. The Basic Properties of Gold Nanoparticles and their Applications in Tumor Diagnosis and Treatment. *Int. J. Mol. Sci.* **2020**, *21*, 2480.

(4) Yang, W.; Liang, H.; Ma, S.; Wang, D.; Huang, J. Gold nanoparticle based photothermal therapy: Development and application for effective cancer treatment. *Sustain. Mater. Technol.* **2019**, *22*, 1–29.

(5) Sztandera, K.; Gorzkiewicz, M.; Klajnert-Maculewicz, B. Gold nanoparticles in cancer treatment. *Mol. Pharmaceutics* **2019**, *16*, 1–23.

(6) Lim, Z.-Z. J.; Li, J.-E. J.; Ng, C.-T.; Yung, L.-Y. L.; Bay, B.-H. Gold nanoparticles in cancer therapy. *Acta Pharmacol. Sin.* **2011**, *32*, 983–990.

(7) Poole, L. B. The basics of thiols and cysteines in redox biology and chemistry. *Free Radic. Biol. Med.* **2015**, *80*, 148–157.

(8) Mirkin, C. A.; Letsinger, R. L.; Mucic, R. C.; Storhoff, J. J. A DNA-based method for rationally assembling nanoparticles into macroscopic materials. *Nature* **1996**, *382*, 1–23.

(9) Zhang, X.; Servos, M. R.; Liu, J. Instantaneous and Quantitative Functionalization of Gold Nanoparticles with Thiolated DNA Using a pH-Assisted and Surfactant-Free Route. *J. Am. Chem. Soc.* **2012**, *134*, 7266–7269.

(10) Peng, C.; Yu, M.; Zheng, J. In Situ Ligand-Directed Growth of Gold Nanoparticles in Biological Tissues. *Nano Lett.* **2020**, *20*, 1378–1382.

(11) Sibuyi, N. R. S.; Moabelo, K. L.; Fadaka, A. O.; Meyer, S.; Onani, M. O.; Madiehe, A. M.; Meyer, M. Multifunctional Gold Nanoparticles for Improved Diagnostic and Therapeutic Applications: A Review. *Nanoscale Res. Lett.* **2021**, *16*, 1–27.

(12) Lee, J.-W.; Soonsanga, S.; Helmann, J. D. A complex thiolate switch regulates the Bacillus-subtilisorganic peroxide sensor OhrR. *PNAS* **2007**, *4*, 8743–8748.

(13) Felice, R. D.; Selloni, A. Adsorption modes of cysteine on Au(111): Thiolate, amino-thiolate, disulfide. *J. Chem. Phys.* **2004**, *120*, 4906–4914.

(14) Yao, G.; Huang, Q. DFT and SERS Study of L-Cysteine Adsorption on the Surface of Gold Nanoparticles. *J. Phys. Chem. C* **2018**, *122*, 15241–15251.

(15) Monti, S.; Carravetta, V.; Ågren, H. Decoration of gold nanoparticles with cysteine in solution: reactive molecular dynamics simulations. *Nanoscale* **2016**, *8*, 12929–12938.

(16) Li, Z. P.; Duan, X. R.; Liu, C. H.; Du, B. A. Selective determination of cysteine by resonance light scattering technique based on self-assembly of gold nanoparticles. *Anal. Biochem.* **2006**, *351*, 18–25.

(17) Matthiesen, J. E.; Jose, D.; Sorensen, C. M.; Klabunde, K. J. Loss of Hydrogen upon Exposure of Thiol to Gold Clusters at Low Temperature. *J. Am. Chem. Soc.* **2012**, *134*, 9376–9379.

(18) Woehrle, G. H.; Brown, L. O.; Hutchison, J. E. Thiol-Functionalized, 1.5-nm Gold Nanoparticles through Ligand Exchange Reactions: Scope and Mechanism of Ligand Exchange. *J. Am. Chem. Soc.* **2005**, *127*, 2172–2183.

(19) Brust, M.; Walker, M.; Bethell, D.; Schiffrin, D. J.; Whyman, R. Synthesis of Thiol-derivatised Gold Nanoparticles in a Two-phase Liquid-Liquid System. *J. Chem. Soc. Commun.* **1994**, *7*, 801–802.

(20) Zalipsky, S. Chemistry of polyethylene glycol conjugates with biologically active molecules. *Adv. Drug Deliv. Rev.* **1995**, *16*, 157–182.

(21) Kou, Z.; Wang, X.; Yuan, R.; Chen, H.; Zhi, Q.; Gao, L.; Wang, B.; Guo, Z.; Xue, X.; Cao, W. et al. A promising gene delivery system developed from PEGylated MoS_2 nanosheets for gene therapy. *Nanoscale Res. Lett.* **2014**, *9*, 587.

(22) Feng, L.; Yang, X.; Shi, X.; Tan, X.; Peng, R.; Wang, J.; Liu, Z. Polyethylene Glycol and Polyethylenimine DualFunctionalized Nano-Graphene Oxide for Photothermally Enhanced Gene Delivery. *Small* **2013**, *9*, 1989–1997.

(23) Chen, L.; Chen, C.; Chen, W.; Li, K.; Chen, X.; Tang, X.; Xie, G.; Luo, X.; Wang, X.; Liang, H. et al. Biodegradable Black Phosphorus Nanosheets Mediate Specific Delivery of hTERT siRNA for Synergistic Cancer Therapy. *ACS Appl. Mater. Interfaces* **2018**, *10*, 21137–21148.

(24) Harikrishna, H.; Ducker, W. A.; Huxtable, S. T. The influence of interface bonding on thermal transport through solid-liquid interfaces. *Appl. Phys. Lett.* **2013**, *102*, 251606.

(25) Stocker, K. M.; Gezelter, J. D. Simulations of Heat Conduction at Thiolate-Capped Gold Surfaces: The Role of Chain Length and Solvent Penetration. *J. Phys. Chem. C* **2013**, *117*, 7605–7612.

(26) Stocker, K. M.; Neidhart, S. M.; Gezelter, J. D. Interfacial thermal conductance of thiolate-protected gold nanospheres. *J. Appl. Phys.* **2016**, *119*, 025106.

(27) Kuang, S.; Gezelter, J. Simulating Interfacial Thermal Conductance at Metal-Solvent Interfaces: The Role of Chemical Capping Agents. *J. Phys. Chem. C* **2011**, *115*, 22475–22483.

(28) Neidhart, S.; Gezelter, J. Thermal Conductivity of Gold-Phenylethanethiol (Au144PET60) Nanoarrays: A Molecular Dynamics Study. *J. Phys. Chem.* **2020**, *124*, 3389–3395.

(29) Salassi, S.; Cardellini, A.; Asinari, P.; Ferrando, R.; Rossi, G. Water dynamics affects thermal transport at the surface of hydrophobic and hydrophilic irradiated nanoparticles. *Nanoscale Adv.* **2020**, *2*, 3181–3190.

(30) Hung, S.-W.; Kikugawa, G.; Shiomi, J. Mechanism of Temperature Dependent Thermal Transport across the Interface between Self-Assembled Monolayer and Water. *J. Phys. Chem. C* **2016**, *102*, 26678–26685.

(31) Tascini, A. S.; Armstrong, J.; Chiavazzo, E.; Fasano, M.; Asinari, P.; Bresme, F. Thermal transport across nanoparticle-fluid interfaces: the interplay of interfacial curvature and nanoparticle-fluid interactions. *Phys. Chem. Chem. Phys.* **2017**, *19*, 3244–3253.

(32) Jiang, M.; Olarte-Plata, J. D.; Bresme, F. Heterogeneous thermal conductance of nanoparticle-fluid interfaces: An atomistic nodal approach. *J. Chem. Phys.* **2022**, *156*, 044701.

(33) Stocker, K.; Gezelter, J. A Method for Creating Thermal and Angular Momentum Fluxes in Nonperiodic Simulations. *J. Chem. Theory Comput.* **2014**, *10*, 1878–1886.

(34) Wilson, B. A.; Nielsen, S. O.; Randrianalisoa, J. H.; Qin, Z. Curvature and temperature-dependent thermal interface conductance between nanoscale gold and water. *J. Chem. Phys.* **2022**, *157*, 054703.

(35) Paniagua-Guerra, L. E.; Ramos-Alvarado, B. Thermal transport across flat and curved gold-water interfaces: Assessing the effects of the interfacial modeling parameters. *J. Chem. Phys.* **2023**, *158*, 134717.

(36) Gutiérrez-Varela, O.; Merabia, S.; Santamaria, R. Size-dependent effects of the thermal transport at gold nanoparticle-water interfaces. *J. Chem. Phys.* **2022**, *157*, 084702.

(37) Pandey, H. D.; Leitner, D. M. Thermalization and Thermal Transport in Molecules. *J. Phys. Chem. Lett.* **2016**, *7*, 5062–5067.

(38) Bhattarai, H.; Newman, K.; Gezelter, J. Polarizable potentials for metals: The density readjusting embedded atom method (DR-EAM). *Phys. Rev. B* **2019**, *99*, 094106.

(39) Bhattarai, H.; Newman, K.; Gezelter, J. The role of polarizability in the interfacial thermal conductance at the gold-water interface. *J. Chem. Phys.* **2020**, *153*, 204703.

(40) Shavalier, S. A.; Gezelter, J. D. Thermal Transport in Citrate-Capped Interfaces Using a Polarizable Force Field. *J. Phys. Chem. C* **2022**, *126*, 12742–12754.

(41) Kuang, S.; Gezelter, J. Velocity shearing and scaling RNEMD: a minimally perturbing method for simulating temperature and momentum gradients. *Mol. Phys.* **2012**, *110:9-10*, 691–701.

(42) Zhou, X.; Johnson, R.; Wadley, H. Misfit-energy-increasing dislocations in vapor-deposited CoFe/NiFe multilayers. *Phys. Rev. B* **2004**, *69*, 144113.

(43) Berendsen, H.; Grigera, J.; Straatsma, T. The Missing Term in Effective Pair Potentials. *J. Phys. Chem.* **1987**, *91*, 6269–6271.

(44) Lubna, N.; Kamath, G.; Potoff, J. J.; Rai, N.; Siepmann, J. I. Transferable Potentials for Phase Equilibria. 8. United-Atom Description for Thiols, Sulfides, Disulfides, and Thiophene. *J. Phys. Chem. B* **2005**, *109*, 24100–24107.

(45) Chen, B.; Potoff, J. J.; Siepmann, J. I. Monte Carlo Calculations for Alcohols and Their Mixtures with Alkanes. Transferable Potentials for Phase Equilibria. 5. United-Atom Description of Primary, Secondary, and Tertiary Alcohols. *J. Phys. Chem. B* **2001**, *105*, 3093–3104.

(46) Stubbs, J. M.; Potoff, J. J.; Siepmann, J. I. Transferable Potentials for Phase Equilibria. 6. United-Atom Description for Ethers, Glycols, Ketones, and Aldehydes. *J. Phys. Chem. B* **2004**, *108*, 17596–17605.

(47) Weiner, S. J.; Kollman, P. A.; Nguyen, D. T.; Case, D. A. An all atom force field for simulations of proteins and nucleic acids. *J. Comp. Chem.* **1986**, *7*, 230–252.

(48) Jorgensen, W. L.; Maxwell, D. S.; Tirado-Rives, J. Development and Testing of the OPLS

All-Atom Force Field on Conformational Energetics and Properties of Organic Liquids. *J. Am. Chem. Soc.* **1996**, *118*, 11225–11236.

(49) Schapotschnikow, P.; Pool, R.; Vlugt, T. J. H. Selective adsorption of alkyl thiols on gold in different geometries. *Comp. Phys. Comm.* **2007**, *177*, 154–157.

(50) Dou, Y.; Zhigilei, L. V.; Winograd, N.; Garrison, B. J. Explosive Boiling of Water Films Adjacent to Heated Surfaces: A Microscopic Description. *J. Phys. Chem. A* **2001**, *105*, 2748–2755.

(51) Martínez, L.; Andrade, R.; Birgin, E.; Martínez, J. Packmol: A package for building initial configurations for molecular dynamics simulations. *J. Chem. Comput.* **2009**, *30(13)*, 2157–2164.

(52) Hoover, W. G. Canonical dynamics: Equilibrium phase-space distributions. *Phys. Rev. A* **1985**, *31*, 1695–1697.

(53) Melchionna, S.; Ciccotti, G.; Holian, B. L. Hoover NPT dynamics for systems varying in shape and size. *Mol. Phys.* **1993**, *78*, 533–544.

(54) Vardeman, C. F.; Stocker, K. M.; Gezelter, J. D. The Langevin Hull: Constant Pressure and Temperature Dynamics for Nonperiodic Systems. *J. Chem. Theory Comput.* **2011**, *7*, 834–842.

(55) Gezelter, J.; Bhattarai, H.; Drisko, C.; Duraes, A.; Lin, T.; Vardeman, C.; Fennell, C.; Meineke, M.; Louden, P.; Neidhart, S. et al. *OpenMD, an Open Source Engine for Molecular Dynamics*, Version 2.7; http://openmd.org. Accessed December 2, 2022.

(56) Swartz, E.; Pohl, R. Thermal boundary resistance. *Rev. Mod. Phys.* **1989**, *61*, 605–668.

(57) Monachon, C.; Weber, L.; Dames, C. Thermal Boundary Conductance: A Materials Science Perspective. *Annu. Rev. Mater. Res.* **2016**, *46*, 433–463.

TOC Graphic

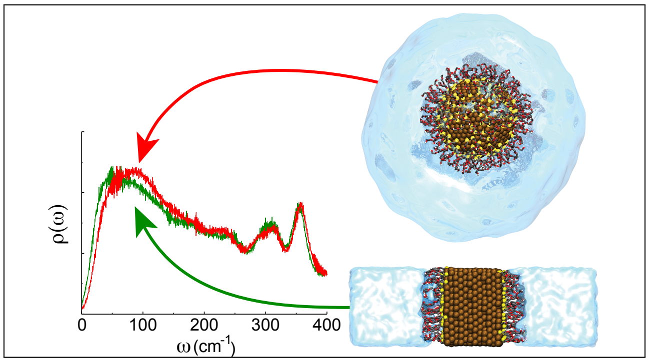

Supporting Information: Heat Transfer in Gold Interfaces Capped with Thiolated Polyethylene Glycol: A Molecular Dynamics Study

Sydney A. Shavalier and J. Daniel Gezelter*

251 Nieuwland Science Hall, Department of Chemistry and Biochemistry,
University of Notre Dame, Notre Dame, Indiana 46556

E-mail: gezelter@nd.edu

Abstract

This supporting document provides details of the force field parameters, information on simulation construction and composition, method validation, and equilibration details for systems described in the accompanying paper. We also include vibrational power spectra for all system components, Bhattacharyya coefficients computed from vibrational power spectra, thermal profiles, mass densities, and charge densities near the interfaces of all polarizable systems.

System Details

This section contains parameters for non-bonded interactions (Table S1), a soft sphere repulsive interaction (Table S2), harmonic bonds (Table S3), harmonic bends (Table S4), torsions (Table S5), embedded atom method (EAM) parameters (Tables S6 and S7), and density-readjusting embedded atom method (DR-EAM) parameters (Table S8).

Force Fields

The thiolated polyethylene glycol (PEG) interaction parameters are taken from previous force fields describing ethers[S1] and various thiols.[S2,S3] We use nonbonded interactions,[S1–S3] harmonic bonds,[S1,S4–S6] harmonic bends,[S1,S2,S5,S6] and both TraPPE[S1,S2,S5,S6] and CHARMM[S1,S5,S6] torsions to describe the thiolated PEG molecules. The atom types for thiolated PEG are shown in Figure S1. To prevent unphysical collisions between the hydroxyl hydrogen (HO) and ether oxygens (OC), an additional soft sphere (r^{-12}) repulsion is added between these two atom types.

Rigid SPC/E water is used as a solvent in this work. The interactions between water and gold are identical to our previous work.[S7] These interaction parameters yield an E_{abs} = -19.5 kJ/mol for water on a (111) gold surface, which is comparable to DFT calculations.[S8]

As pair potentials alone are not sufficient to describe the many-atom properties of metals, we use EAM parameters from Zhou *et al.* for gold in non-polarizable systems.[S9] We use DR-

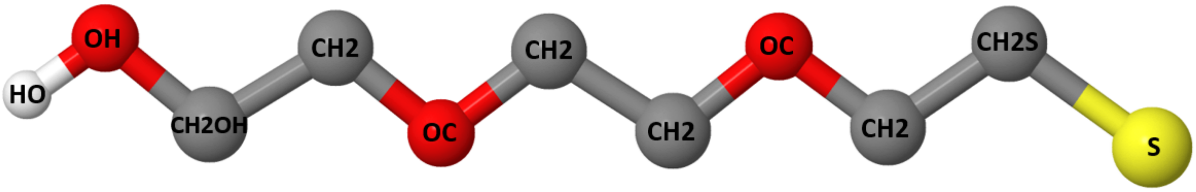

Figure S1: thiolated PEG atom types. Carbon atoms are gray, oxygen atoms are red, sulfur is yellow, and the explicit hydrogen is white. All other hydrogen atoms are treated implicitly.

EAM parameters from Bhattarai *et al.* for gold in polarizable systems.[S10] The damped shifted force model from Fennell and Gezelter was used for long-range electrostatic interactions with a damping parameter, $\alpha = 0.18$ Å^{-1}, which yields good agreement with Ewald electrostatics when $r_{\text{cut}} = 12$ Å.[S11]

Table S1: Non-bonded interactions used for simulations of gold nanostructures and thiolated PEG in a water solvent. All parameters listed are Lennard-Jones $n-m$ pairwise terms. The $\varepsilon_{\mathrm{Au}-i}$ values for water have been modified from Dou *et al.*[S12] to more closely replicate the adsorption energy for water on a (111) gold surface determined by DFT calculations.[S8] The cross interactions containing HO and H-SPCE are purely repulsive.

Atom	Mass (au)	σ_{ii} (Å)	ε_{ii} (kcal/mol)	$\sigma_{\mathrm{Au}-i}$ (Å)	$\varepsilon_{\mathrm{Au}-i}$ (kcal/mol)	n	m	Charge (e)	Source
Au	196.97	-	-	-	-	-	-	0.0	
CH2	14.03	3.95^{a}	0.0914^{a}	3.54^{b}	0.175^{b}	12	6	0.250^{a}	Refs. $S1^{a}$, $S3^{b}$
CH2OH	14.03	3.95^{a}	0.0914^{a}	3.54^{b}	0.175^{b}	12	6	0.265^{a}	Refs. $S1^{a}$, $S3^{b}$
CH2S	14.03	3.95^{a}	0.0914^{a}	3.54^{b}	0.175^{b}	12	6	0.171^{a}	Refs. $S2^{a}$, $S3^{b}$
OH	15.9994	3.02^{a}	0.1848^{a}	$3.12^{a,b}$	$0.213^{a,b}$	12	6	-0.700^{a}	Refs. $S1^{a}$, $S3^{b}$
HO	1.0079	0.0	0.0	1	79487.7^{a}	12	-	0.435^{a}	Ref. S1
OC	15.9994	2.80^{a}	0.1093^{a}	$3.01^{a,b}$	$0.164^{a,b}$	12	6	-0.500^{a}	Refs. $S1^{a}$, $S3^{b}$
S	32.0655	3.62^{a}	0.4610^{a}	2.65^{b}	5.554^{b}	12	6	-0.171^{a}	Refs. $S2^{a}$, $S13^{b}$
O−SPCE	15.9994	3.16549^{a}	0.15532^{a}	3.18284	0.6285748	9	6	-0.848	Refs. S14, S15
H−SPCE	1.0079	0.0	0.0	1	0.0008492	4	-	0.424	Refs. S14, S15

Table S2: Repulsive soft sphere (r^{-12}) interaction between the hydroxyl hydrogen and non-terminal ether oxygen (OC) atoms in the thiolated PEG.

i	j	σ_{ij} (Å)	ε_{ij} (kcal/mol)	n	Source
HO	OC	1	79487.7	12	Ref. S1

Table S3: Harmonic bond parameters for thiolated PEG. Water is simulated as a rigid body so no harmonic bond parameters are needed.

i	j	r_0 (Å)	K_{ij} (kcal/mol × Å^2)	Source
CH2	OC	1.41[a]	640.0[b]	Refs. S1[a], S4[b]
CH2	CH2	1.54[a]	536.0[b]	Refs. S1[a], S16[b]
CH2	CH2S	1.54[a]	536.0[b]	Refs. S1[a], S16[b]
OH	HO	0.945[a]	553.0[b]	Refs. S6[a], S4[b]
S	CH2S	1.81	444.0	Ref. S4
CH2OH	CH2	1.54[a]	536.0[b]	Refs. S1[a], S16[b]
OH	CH2OH	1.41[a]	640.0[b]	Refs. S1[a], S4[b]

Table S4: Harmonic bend parameters for thiolated PEG. The central atom in each bend is atom j, bonded to atoms i and k.

i	j	k	θ_0 (degrees)	K_{ijk} (kcal/mol × rad^2)	Source
HO	OH	CH2OH	108.5	110.0844	Ref. S6
CH2	CH2	OC	112.0	99.9503	Ref. S1
CH2	OC	CH2	112.0	120.0198	Ref. S1
CH2	CH2S	S	114.7	100.0	Ref. S2
OH	CH2OH	CH2	109.5	100.1490	Ref. S6
CH2OH	CH2	OC	112.0	99.9503	Ref. S1
OC	CH2	CH2S	112.0	99.9503	Ref. S2

Table S5: TraPPE torsions for thiolated PEG which have the form $V_{\text{torsion}}(\phi) = c_0 + c_1(1 + \cos\phi) + c_2(1 - \cos 2\phi) + c_3(1 + \cos 3\phi)$.

i	j	k	l	c_0	c_1	c_2	c_3	Source
CH2	CH2OH	OH	HO	0.0	0.4169	-0.0580	0.3734	Ref. S6
CH2	CH2	OC	CH2	0.0	1.4413	-0.3254	1.1092	Ref. S1
OC	CH2	CH2	OC	1.0	0.0	-0.500	2.0	Ref. S1
S	CH2S	CH2	OC	1.0	0.0	-0.500	2.0	Ref. S2
OH	CH2OH	CH2	OC	1.0	0.0	-0.500	2.0	Ref. S1
CH2OH	CH2	OC	CH2	0.0	1.441	-0.325	1.109	Ref. S2
CH2	OC	CH2	CH2S	0.0	1.441	-0.325	1.109	Ref. S2

Table S6: Gold EAM parameters for $\phi(r)$ and $f(r)$. $\phi(r)$ is a generalized elemental pair potential. The electron density function $f(r)$ has the same form as the attractive portion of $\phi(r)$.

$$\phi(r) = \frac{\mathbf{A}\mathbf{exp}[-\alpha(\frac{r}{r_e}-1)]}{1+(\frac{r}{r_e}-\kappa)} - \frac{\mathbf{B}\mathbf{exp}[-\beta(\frac{r}{r_e}-1)]}{1+(\frac{r}{r_e}-\lambda)^{20}};$$

$$f(r) = \frac{f_e\mathbf{exp}[-\beta(\frac{r}{r_e}-1)]}{1+(\frac{r}{r_e}-\lambda)^{20}}.$$

r_e(Å)	f_e(eV/Å)	ρ_e(eV/Å)	ρ_s(eV/Å)	α	β	A	B	κ	λ	Source
2.885034	1.529021	19.991632	19.991509	9.516052	5.075228	0.229762	0.356666	0.35657	0.748798	Ref. S9

Table S7: Gold EAM parameters for the embedding function $F(\rho)$. The three equations below allow the calculation of $F(\rho)$ at three different electron density ranges:

$F(\rho) = \sum_{i=0}^{3} F_{ni}(\frac{\rho}{\rho_n} - 1)^i$, $\rho < \rho_n, \rho_n = 0.85\rho_e$;

$F(\rho) = \sum_{i=0}^{3} F_i(\frac{\rho}{\rho_e} - 1)^i$, $\rho_n \leq \rho < \rho_0, \rho_0 = 1.15\rho_e$;

$F(\rho) = F_e[1 - ln(\frac{\rho}{\rho_s})^\eta](\frac{\rho}{\rho_s})^\eta$, $\rho < \rho_n, \rho_0 \leq \rho$.

F_{n0}	F_{n1}	F_{n2}	F_{n3}	F_0	F_1	F_2	F_3	F_e	η	Source
– 2.937772	-0.500288	1.601954	-0.835530	-2.98	0	1.706587	-1.134778	-2.978815	1.021095	Ref. S9

Table S8: Gold DR-EAM self-potential parameters. The chargeMass term is a tunable parameter that determines the speed at which the polarizable gold atom responds to an external field. N_{eff} describes the effective number of charge carriers per gold atom. All parameter units result in a self-potential in eV. The self-potential is described by $V_{self}(q) = \sum_{n=1}^{6} a_n q^n$.

chargeMass	N_{eff}	a_1	a_2	a_3	a_4	a_5	a_6	Source
1000.0	0.59	13.89	7.92	13.192055	68.173897	-88.029873	28.855093	Ref. S10

System Preparation and Equilibration

Planar gold slabs ($a = 4.08$Å) exposing the (111), (110), and (100) facets were built with slabBuilder, an OpenMD utility that rotates the specified facet so that it is positioned normal to the z-axis of the simulation cell.[S17] An identically-sized solvent box was constructed using Packmol[S18] and OpenMD,[S17] and the thiolated PEG positions were randomized in each statistically-independent replica (with four replicas for each studied interface).

The spherical gold nanoparticles used in all non-periodic simulations were built with a lattice constant of 4.08 Å using nanoparticleBuilder, another OpenMD utility.[S17] These particles were constructed with a radius of either 10 or 20 Å. The gold nanoparticle underwent structural relaxation with incremental temperature increases up to 300 K. The solvent spheres were created with empty center regions to allow for simplified merging with the gold nanoparticles. One gold atom at the center of the spherical nanoparticle was given a large mass ($m = 1.9697 \times 10^6$ amu) to prevent nanoparticle drifting.

For all systems, the metal and solvent layers were combined using other OpenMD utilities, and steepest descent optimization was used to structurally relax each system. Particle velocities were resampled from a Maxwell-Boltzmann distribution at 300 K prior to equilibration.[S17] The structural makeup of each system studied is shown in Table S9.

All systems using the DR-EAM metal potential were simulated directly prior to equilibration using a time step of 0.2 fs, as the charge degrees of freedom in DR-EAM must be simultaneously propagated. A time step of 1 fs was used for all equilibration and flux application steps.

Table S9: Structures simulated in this work

	Spheres		Slabs		
	10 Å	20 Å	(111)	(110)	(100)
Metallic structure (in Å)	$r = 10$	$r = 20$	$31 \times 36 \times 28$	$30 \times 35 \times 29$	$30 \times 36 \times 29$
Total System size (in Å)	$r \sim 40$	$r \sim 50$	$31 \times 36 \times 117$	$30 \times 35 \times 120$	$30 \times 36 \times 118$
Gold volume (Å^3)	4,189	33,510	29,340	28,525	28,525
Solvent volume (Å^3)	175,406	490,088	101,250	97,900	101,030
N_{Gold}	249	1985	1728	1680	1680
N_{Water}	6018	17,024	2854	2790	2790
$N_{\text{thiolatedPEG}}$	59	234	104	98	100
$\rho_{\text{thiolatedPEG}}$ (nm^{-2})	4.70	4.66	4.81	4.67	4.63

The planar systems were first structurally relaxed (NVT), followed by a pressure correction (NPT) with separate barostats for each dimension. This was followed by thermal relaxation (NVT) and equilibration using a microcanonical integrator (NVE). The planar systems were simulated using periodic boundary conditions. The spherical systems were equilibrated for 250 ps using the non-periodic Langevin Hull integrator[S19] and velocity resampling at 300 K every ps, and then an additional 200 ps with no resampling.

After equilibration, a thermal flux was applied to each system using the velocity shearing and scaling reverse non-equilibrium molecular dynamics (VSS-RNEMD) methods developed by Kuang and Gezelter.[S20] A flux was applied until thermal gradients and temperature discontinuities developed. Kinetic energy was exchanged between either two slabs separated in z (planar systems) or two concentric spherical shells (spherical systems). The thermal flux was applied for 5 ns in all systems. For planar systems, the thermal data shown in this work was averaged across the entire 5 ns of flux application. For the nanospheres, the thermal data was averaged across the last 1 ns of flux application. Coupling to the thermal bath was removed in spherical systems so as to prevent interference with the applied flux. In polarizable systems, the fluctuating charges were propagated using a microcanonical (NVE) integrator to mitigate unphysical losses of kinetic energy into the electronic degrees of freedom.

In Figure S2, we show that we are in the linear response regime with the applied flux utilized in the main paper. We tested a total of five flux values, and these were applied for 5 ns on a set of Au(111) systems. The flux used for planar systems in this work was 5.0×10^{-6} kcal $\text{mol}^{-1}\text{Å}^{-2}$ fs^{-1} (3500 MW m^{-2}).

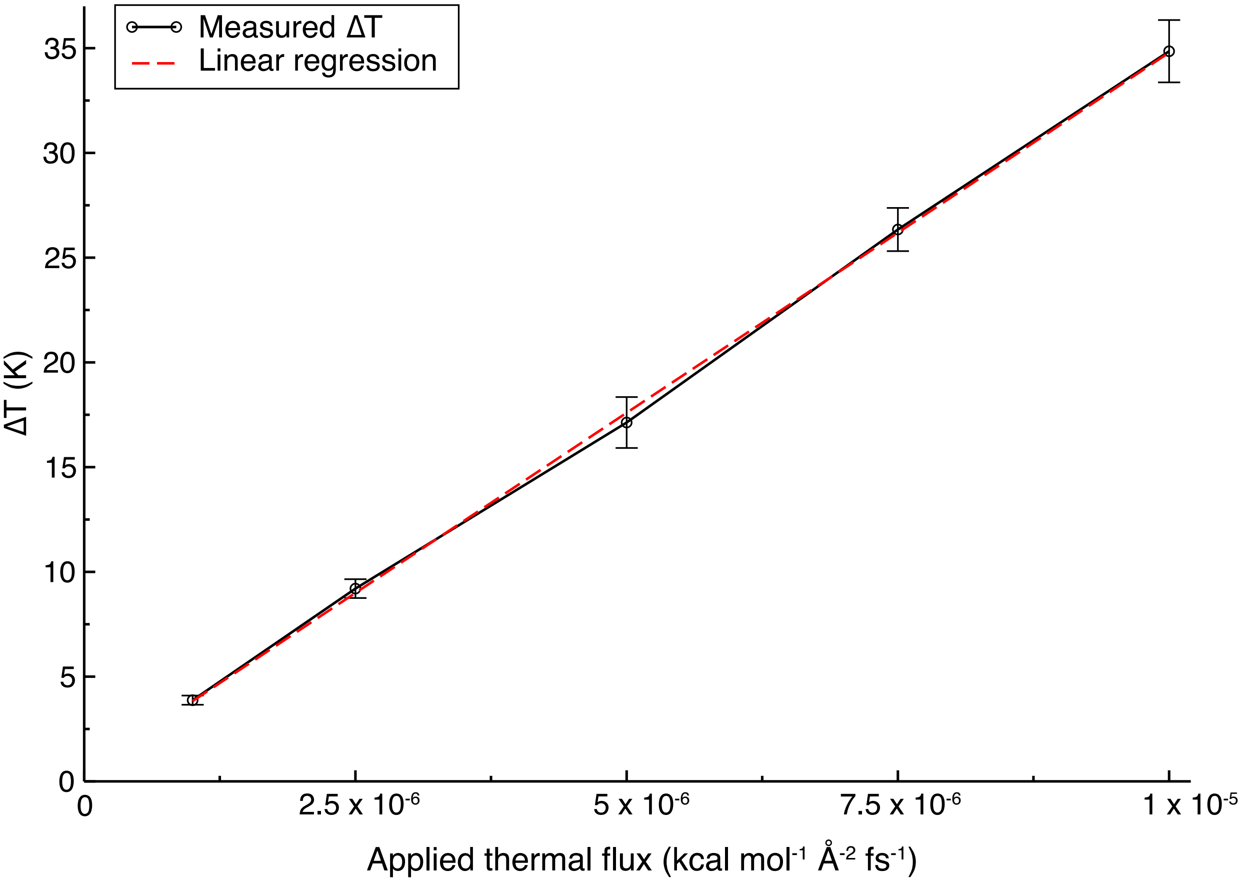

Figure S2: A test of five values of applied flux bracketing the flux used in the main paper. This test is for Au(111) interfaces. Each point is an average of four statistically independent simulations.

Additional Thermal Profiles and Mass Densities

The thermal profiles and local mass densities for all components in polarizable systems are shown in Figures S3 and S4. The temperature drop is largest between gold and sulfur in these systems as in their non-polarizable counterparts. There are no compelling differences between Figure S3 and Figure 2 in the main text, but we note a small decrease in the penetration of sulfur into gold in the polarizable Au(111) surface. The ordering of water molecules near the interface are similar to that of Figure 2. When comparing Figure S4 with Figure 3 in the main text, it is clear that polarizability makes no significant difference in the ordering of any species.

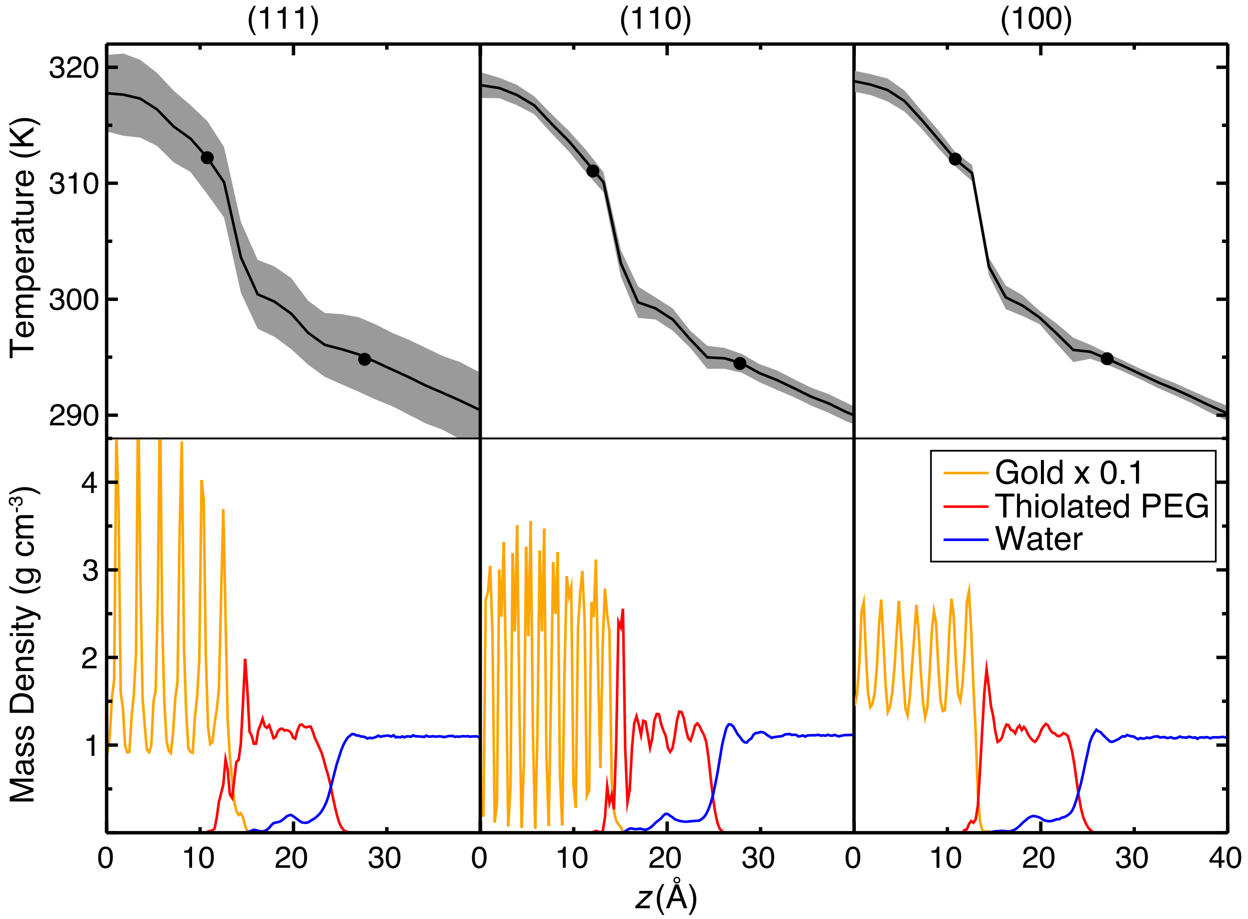

Figure S3: Under an applied thermal flux, temperature drops are largest at the location of the Gold-Sulfur bond. (Top) Thermal profiles of planar systems simulated using the polarizable DR-EAM potential. Shading indicates the 95% confidence interval for computed temperatures, while the black dots are the bounds of the interfacial region used for computing conductance. (Bottom) Mass densities of each species. $z = 0$ represents the center of the gold slabs.

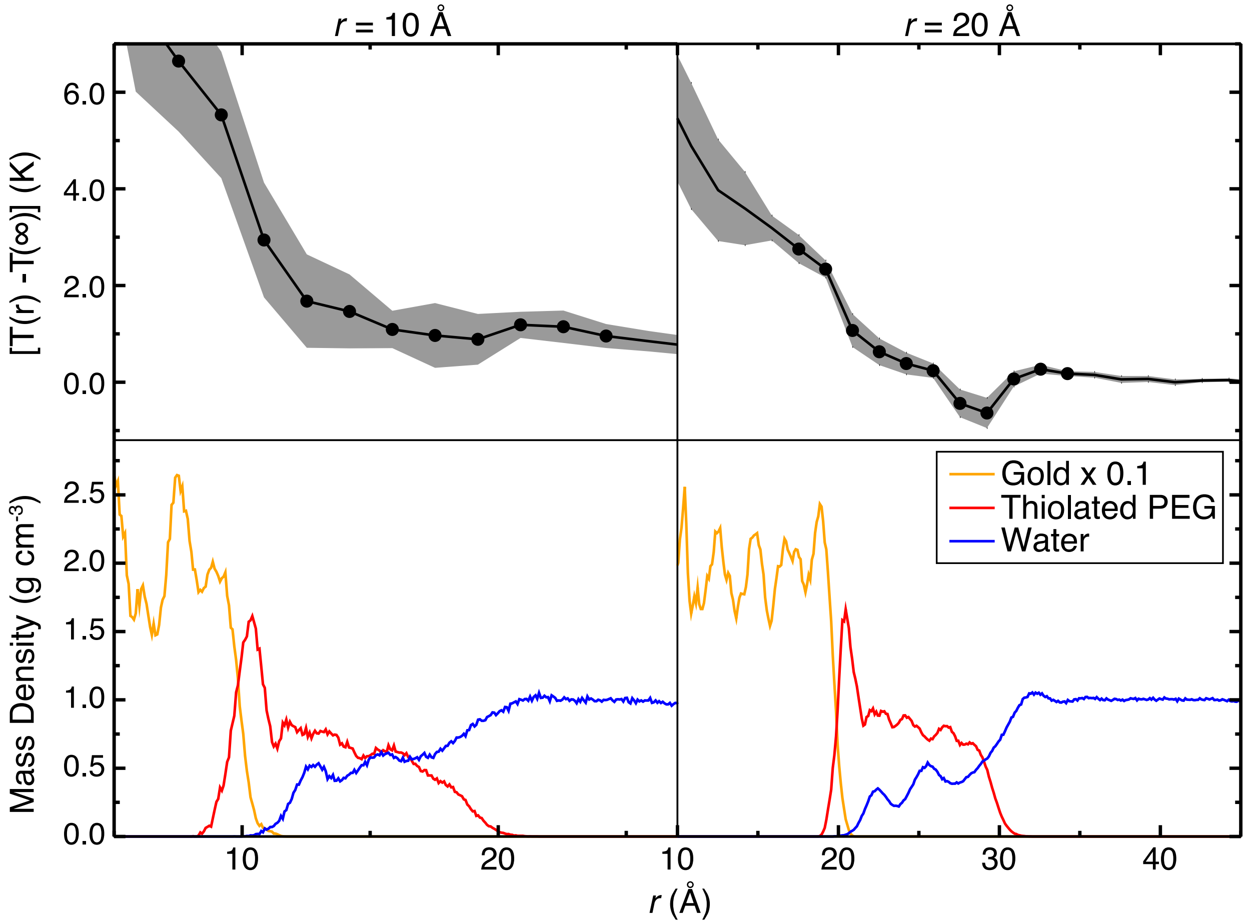

Figure S4: In the nanospheres, temperature drops are also largest at the Gold-Sulfur bond. (Top) Thermal profiles of nanoparticle systems, relative to the temperature of the solvent far from the particle. The shaded region represents the 95% confidence intervals. The black data points are the temperature differences in the Kapitza region which were used for calculating conductance. (Bottom) Local mass densities of each species for the nanoparticles using the polarizable DR-EAM model. $r = 0$ is at the center of the gold nanosphere.

Additional Vibrational Power Spectra

The vibrational power spectra for all components of the planar systems are shown in Figure S5. There are no clear differences across metallic facet or polarizability here. The full gold spectra cannot be seen here, but they do not differ significantly and obscure the other spectra when in full view.

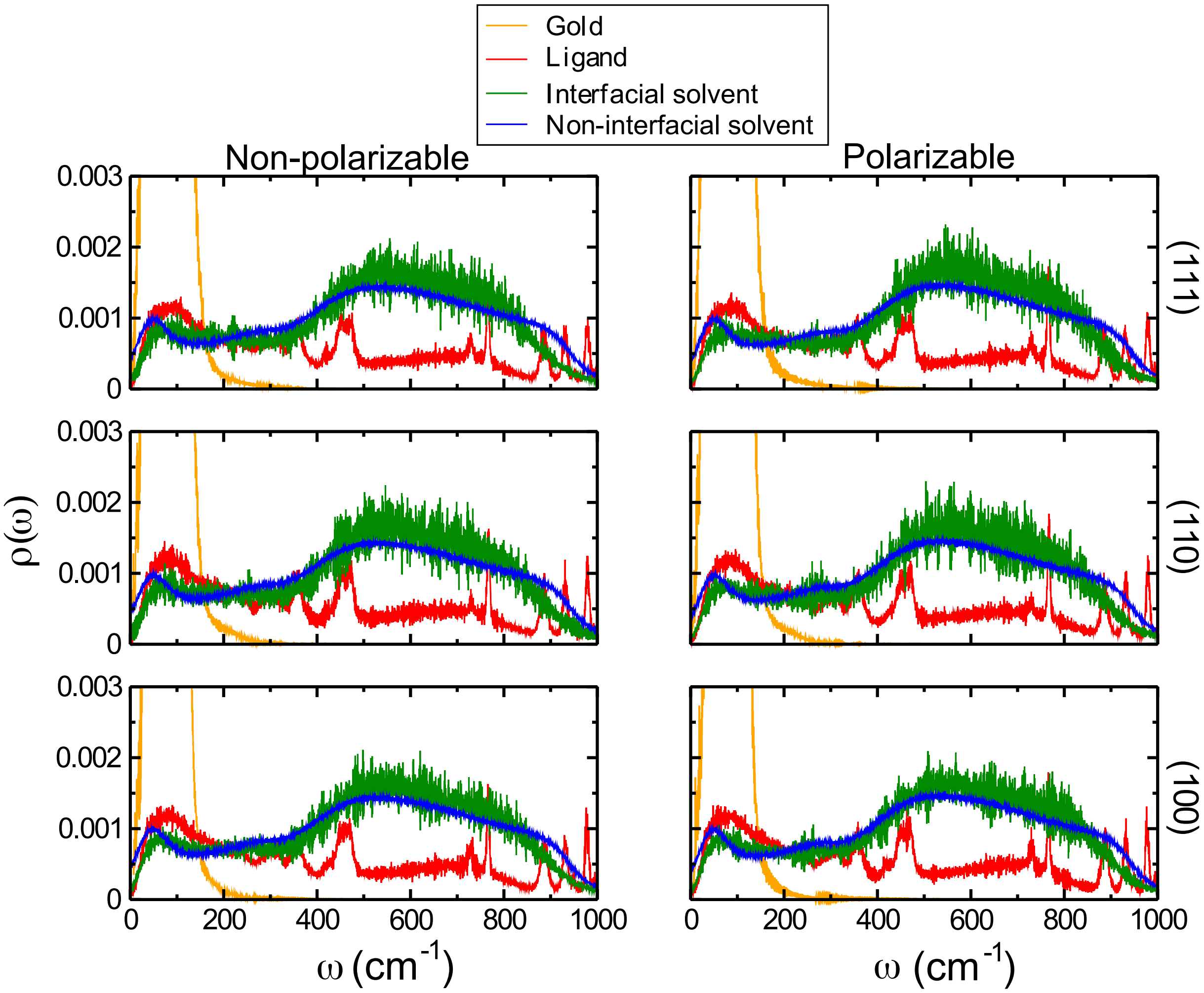

Figure S5: Low frequency portions of the vibrational power spectra for all planar systems studied. Note that the y-axis has been scaled down to allow visualization of the ligand and solvent spectra, and the gold spectra extend beyond the scope of these plots.

The vibrational power spectra for all components of spherical systems are shown in Figure S6. There appears to be little effect of either system size or metal polarizability here as well. Again, the gold spectra do not differ significantly and are thus not fully shown. A full analysis of the differences in spectra between the planar and spherical systems is available in the main text.

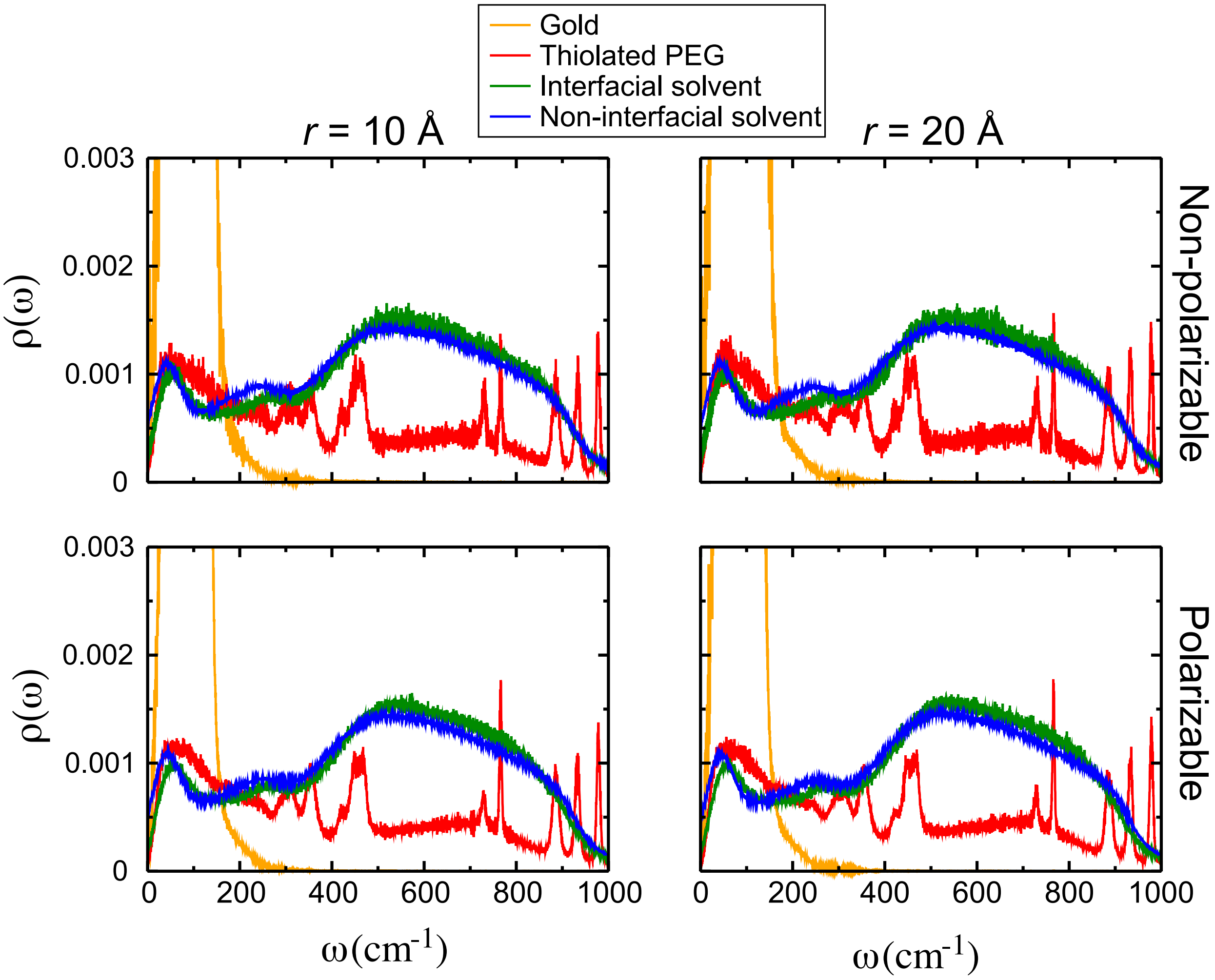

Figure S6: Vibrational power spectra for all spherical systems studied. The y-axis has been scaled as in Fig. S5.

As thiolated PEG exhibits both low and high frequency activity, we have computed the averaged spectra for thiolated PEG in the planar and nanosphere systems which are are shown in Figure S7. Overall, these spectra do not differ significantly. The peak ranging from approximately 3700 - 3900 cm^{-1} is likely an O-H stretch from the terminal hydroxyl group.

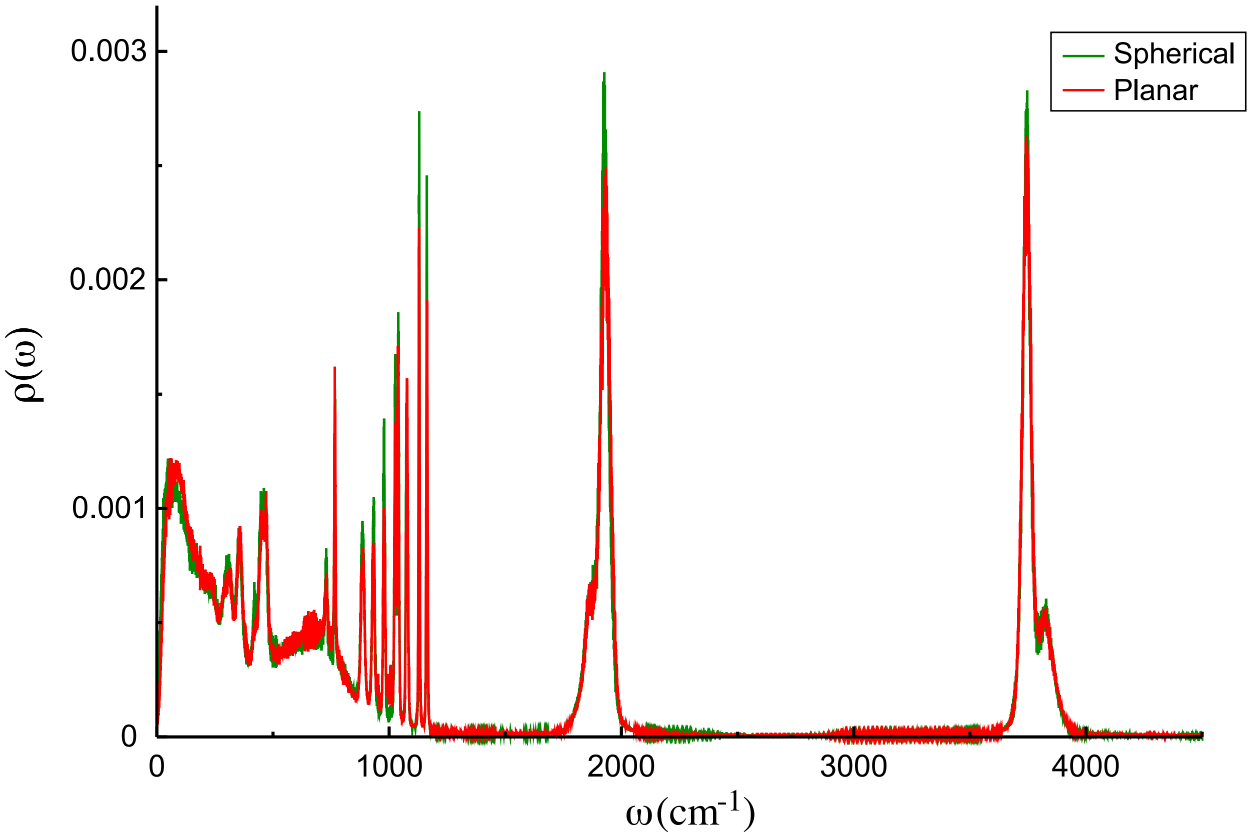

Figure S7: Averaged thiolated PEG vibrational power spectra for planar and spherical systems. Note: the planar curve is an average of all polarizable and non-polarizable (111), (110), and (100) facets, and the spherical curve is an average of all polarizable and non-polarizable nanospheres with radii of 10 and 20 Å.

Additional Bhattacharyya Coefficients

We have also included Bhattacharyya coefficients (BC) which are similar calculations to those in Table 3 but using power spectra rather than mass densitites. The BC values for the thiolated PEG / gold and thiolated PEG / water pairs are shown in Table S10. The water has been categorized into interfacial and bulk regions, where interfacial water comprises solvent molecules that are trapped in the thiolated PEG layer, and bulk water captures the solvent molecules outside that region. The magnitude of BC values are larger for each pair here than those for the same pairs calculated with mass densities. These coefficients appear to be unaffected by metallic polarizability or planar facet, but the mean BC values for the thiolated PEG / gold pair are higher in the 10 Å nanospheres than for the other systems. As expected, there is very little difference between the BCs for bulk and interfacial water, and their power spectra exhibit a significant amount of overlap with that of thiolated PEG. In Table 3, we noted that the BCs for the thiolated PEG-gold pair in the Au(111) systems were about twice as large as those for the Au(110) and Au(100) systems, but that difference does not exist here.

Table S10: Vibrational power spectral overlap measured using Bhattacharyya coefficients, showing the degree of similarity between the thiolated PEG and the other two components of the metal / ligand / water systems.

Facet	Metal	BC with thiolated PEG (unitless)		
		Interfacial water	Bulk water	Gold
(111)	non-polarizable	0.740 ± 0.007	0.737 ± 0.007	0.434 ± 0.007
	polarizable	0.732 ± 0.008	0.741 ± 0.014	0.447 ± 0.013
(110)	non-polarizable	0.737 ± 0.011	0.745 ± 0.007	0.438 ± 0.018
	polarizable	0.735 ± 0.009	0.735 ± 0.002	0.426 ± 0.006
(100)	non-polarizable	0.747 ± 0.007	0.747 ± 0.004	0.424 ± 0.013
	polarizable	0.736 ± 0.007	0.739 ± 0.007	0.423 ± 0.015
NP ($r = 10$ Å)	non-polarizable	0.739 ± 0.015	0.740 ± 0.014	0.452 ± 0.022
	polarizable	0.740 ± 0.011	0.740 ± 0.013	0.452 ± 0.016
NP ($r = 20$ Å)	non-polarizable	0.745 ± 0.004	0.745 ± 0.004	0.429 ± 0.008
	polarizable	0.741 ± 0.005	0.742 ± 0.004	0.427 ± 0.006

Charge Penetration at the Interface

The image charge effect describes the phenomenon in which a metallic species responds to a nearby external charge by inducing the opposite charge on its surface. DR-EAM has previously been shown to replicate this effect in systems of bare gold solvated in water.[S7,S10] To investigate how these systems respond when the gold is polarizable, we calculated the charge density as a function of z (for planar systems) or r (for spherical systems).

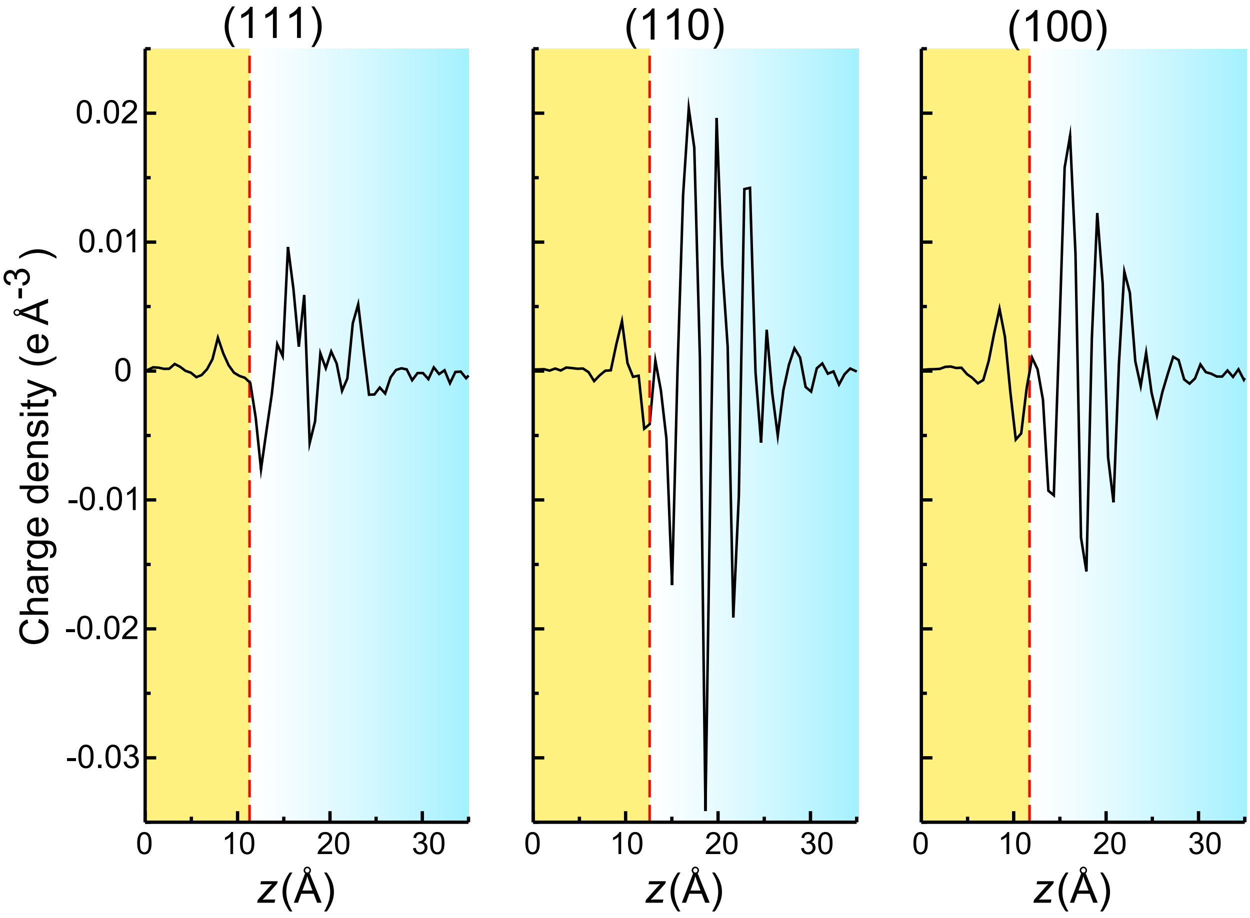

Figure S8: Charge density as a function of z in planar systems using the polarizable metal potential DR-EAM. The dashed red line indicates the gold/thiolated PEG interface in each plot.

Figure S8 shows the charge density as a function of z for planar systems. The positive peak directly to the left of the interface on each plot (dashed red line) represents the positive charge of the surface gold atoms responding to the negatively charged sulfur atoms near the surface. The magnitude of these peaks does not vary significantly, suggesting that the difference in gold atom packing across fcc lattices does not change the ordering of charges at the gold surface. The negative peak directly adjacent to the gold represents the sulfur atoms in the thiolated PEG molecules. Unlike the gold peaks, these vary across gold facets, as does the magnitude of the ether oxygen peaks starting at around 20 Å. This difference in the gold surface disruption likely leads to the differing magnitudes of sulfur and ether oxygen peaks. It is also clear from these plots that the ligand layer is more ordered on the Au(110) and Au(100) facets.

The charge density as a function of r is shown for spherical systems in Figure S9. Here, the magnitude of the first gold peak is approximately equal in both systems, as is the sulfur peak. However, the magnitude of the second gold peak differs greatly, with a much larger magnitude in the smaller systems. Additionally, the ether oxygens appear to be more ordered in systems where the gold radius is 20 Å, with clear ordering out to $r = 30$ Å, the approximate location of the hydroxyl oxygen. In the smaller nanospheres, the thiolated PEG chains have more internal disorder, and the ether oxygen minima are discernible only out to $r = 15$ Å.

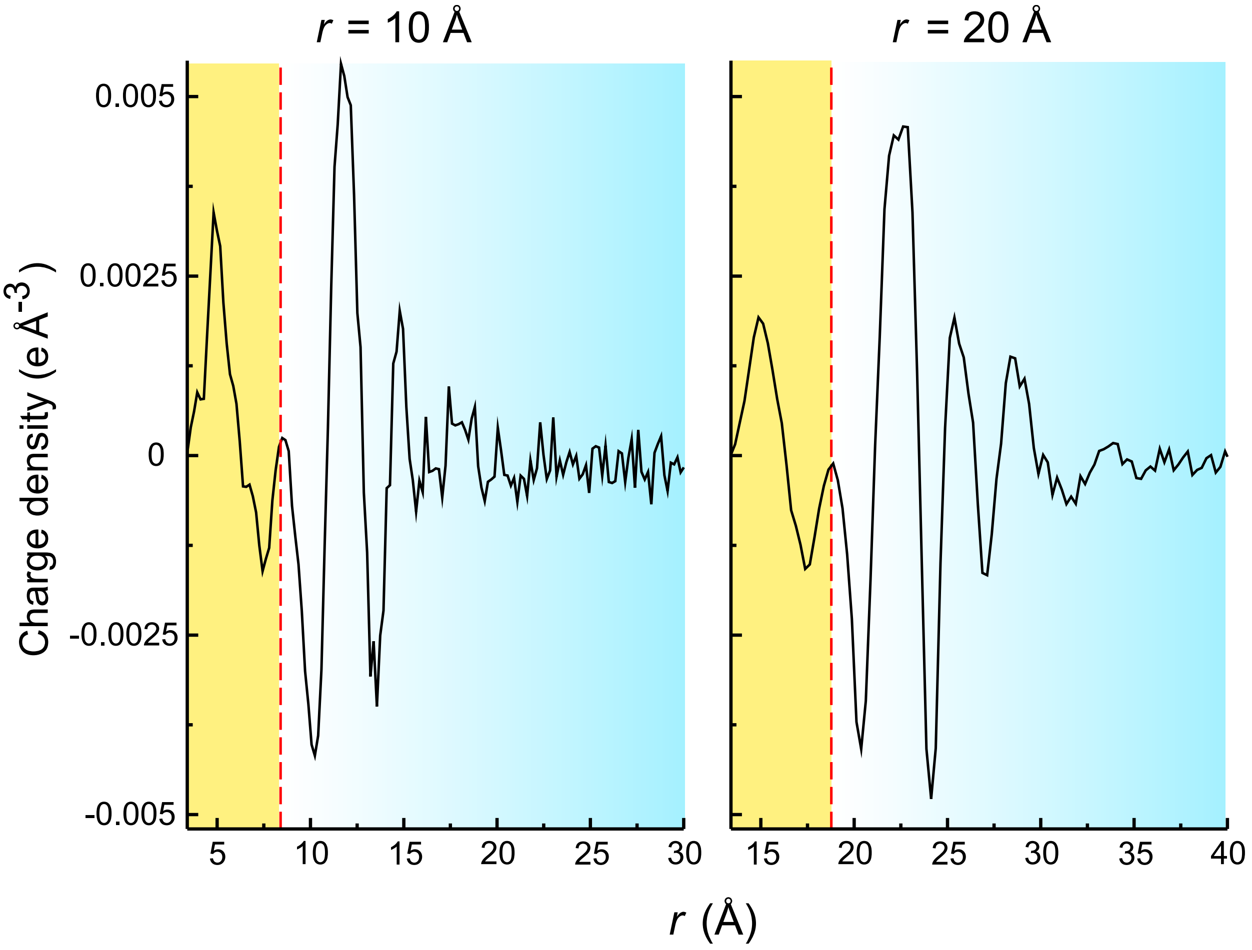

Figure S9: Charge density as a function of r in spherical systems using the polarizable metal potential DR-EAM.

References

(S1) Stubbs, J. M.; Potoff, J. J.; Siepmann, J. I. Transferable Potentials for Phase Equilibria. 6. United-Atom Description for Ethers, Glycols, Ketones, and Aldehydes. *J. Phys. Chem. B* **2004**, *108*, 17596–17605.

(S2) Lubna, N.; Kamath, G.; Potoff, J. J.; Rai, N.; Siepmann, J. I. Transferable Potentials for Phase Equilibria. 8. United-Atom Description for Thiols, Sulfides, Disulfides, and Thiophene. *J. Phys. Chem. B* **2005**, *109*, 24100–24107.

(S3) Schapotschnikow, P.; Pool, R.; Vlugt, T. J. H. Selective adsorption of alkyl thiols on gold in different geometries. *Comp. Phys. Comm.* **2007**, *177*, 154–157.

(S4) Weiner, S. J.; Kollman, P. A.; Nguyen, D. T.; Case, D. A. An all atom force field for simulations of proteins and nucleic acids. *J. Comp. Chem.* **1986**, *7*, 230–252.

(S5) Martin, M. G.; Siepmann, J. I. Transferable Potentials for Phase Equilibria. 1. United-Atom Description of n-Alkanes. *J. Phys. Chem. B* **1998**, *102*, 2569–2577.

(S6) Chen, B.; Potoff, J. J.; Siepmann, J. I. Monte Carlo Calculations for Alcohols and Their Mixtures with Alkanes. Transferable Potentials for Phase Equilibria. 5. United-Atom Description of Primary, Secondary, and Tertiary Alcohols. *J. Phys. Chem. B* **2001**, *105*, 3093–3104.

(S7) Shavalier, S. A.; Gezelter, J. D. Thermal Transport in Citrate-Capped Interfaces Using a Polarizable Force Field. *J. Phys. Chem. C* **2022**, *126*, 12742–12754.

(S8) Berg, A.; Peter, C.; Johnston, K. Evaluation and Optimisation of Interface Force Fields for Water on Gold Surfaces. *J. Chem. Theory Comput.* **2017**, *13*, 5610–5623.

(S9) Zhou, X.; Johnson, R.; Wadley, H. Misfit-energy-increasing dislocations in vapor-deposited CoFe/NiFe multilayers. *Phys. Rev. B* **2004**, *69*, 144113.

(S10) Bhattarai, H.; Newman, K.; Gezelter, J. Polarizable potentials for metals: The density readjusting embedded atom method (DR-EAM). *Phys. Rev. B* **2019**, *99*, 094106.

(S11) Fennell, C.; Gezelter, J. Is the Ewald summation still necessary? Pairwise alternatives to the accepted standard for long-range electrostatics. *J. Chem. Phys.* **2006**, *124*, 234104.

(S12) Dou, Y.; Zhigilei, L. V.; Winograd, N.; Garrison, B. J. Explosive Boiling of Water Films Adjacent to Heated Surfaces: A Microscopic Description. *J. Phys. Chem. A* **2001**, *105*, 2748–2755.

(S13) Pool, R.; Schapotschnikow, P.; Vlugt, T. J. H. Solvent Effects in the Adsorption of Alkyl Thiols on Gold Structures: A Molecular Simulation Study. *J. Phys. Chem. C* **2007**, *111*, 10201–10212.

(S14) Berendsen, H.; Grigera, J.; Straatsma, T. The Missing Term in Effective Pair Potentials. *J. Phys. Chem.* **1987**, *91*, 6269–6271.

(S15) Bhattarai, H.; Newman, K.; Gezelter, J. The role of polarizability in the interfacial thermal conductance at the gold-water interface. *J. Chem. Phys.* **2020**, *153*, 204703.

(S16) Jorgensen, W. L.; Maxwell, D. S.; Tirado-Rives, J. Development and Testing of the OPLS All-Atom Force Field on Conformational Energetics and Properties of Organic Liquids. *J. Am. Chem. Soc.* **1996**, *118*, 11225–11236.

(S17) Gezelter, J.; Bhattarai, H.; Drisko, C.; Duraes, A.; Lin, T.; Vardeman, C.; Fennell, C.; Meineke, M.; Louden, P.; Neidhart, S.; Kuang, S.; Lamichhane, M.; Michalka, J.; Stocker, K.; Marr, J.; Sun, X.; Li, C.; Daily, K.; Zheng, Y. *OpenMD, an Open Source Engine for Molecular Dynamics*, Version 2.7; http://openmd.org. Accessed December 2, 2022.

(S18) Martínez, L.; Andrade, R.; Birgin, E.; Martínez, J. Packmol: A package for building initial configurations for molecular dynamics simulations. *J. Chem. Comput.* **2009**, *30(13)*, 2157–2164.

(S19) Vardeman, C. F.; Stocker, K. M.; Gezelter, J. D. The Langevin Hull: Constant Pressure and Temperature Dynamics for Nonperiodic Systems. *J. Chem. Theory Comput.* **2011**, *7*, 834–842.

(S20) Stocker, K. M.; Gezelter, J. D. Simulations of Heat Conduction at Thiolate-Capped Gold Surfaces: The Role of Chain Length and Solvent Penetration. *J. Phys. Chem. C* **2013**, *117*, 7605–7612.

Supporting Information: Heat Transfer in Gold Interfaces Capped with Thiolated Polyethylene Glycol: A Molecular Dynamics Study

Sydney A. Shavalier and J. Daniel Gezelter*

251 Nieuwland Science Hall, Department of Chemistry and Biochemistry,
University of Notre Dame, Notre Dame, Indiana 46556

E-mail: gezelter@nd.edu

Abstract

This supporting document provides details of the force field parameters, information on simulation construction and composition, method validation, and equilibration details for systems described in the accompanying paper. We also include vibrational power spectra for all system components, Bhattacharyya coefficients computed from vibrational power spectra, thermal profiles, mass densities, and charge densities near the interfaces of all polarizable systems.

System Details

This section contains parameters for non-bonded interactions (Table S1), a soft sphere repulsive interaction (Table S2), harmonic bonds (Table S3), harmonic bends (Table S4), torsions (Table S5), embedded atom method (EAM) parameters (Tables S6 and S7), and density-readjusting embedded atom method (DR-EAM) parameters (Table S8).

Force Fields

The thiolated polyethylene glycol (PEG) interaction parameters are taken from previous force fields describing ethers[S1] and various thiols.[S2,S3] We use nonbonded interactions,[S1–S3] harmonic bonds,[S1,S4–S6] harmonic bends,[S1,S2,S5,S6] and both TraPPE[S1,S2,S5,S6] and CHARMM[S1,S5,S6] torsions to describe the thiolated PEG molecules. The atom types for thiolated PEG are shown in Figure S1. To prevent unphysical collisions between the hydroxyl hydrogen (HO) and ether oxygens (OC), an additional soft sphere (r^{-12}) repulsion is added between these two atom types.

Rigid SPC/E water is used as a solvent in this work. The interactions between water and gold are identical to our previous work.[S7] These interaction parameters yield an E_{abs} = -19.5 kJ/mol for water on a (111) gold surface, which is comparable to DFT calculations.[S8]

As pair potentials alone are not sufficient to describe the many-atom properties of metals, we use EAM parameters from Zhou *et al.* for gold in non-polarizable systems.[S9] We use DR-

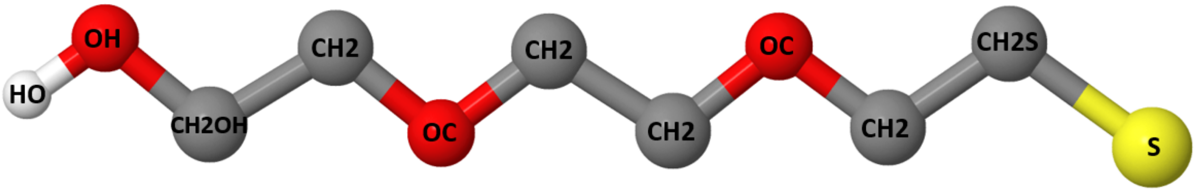

Figure S1: thiolated PEG atom types. Carbon atoms are gray, oxygen atoms are red, sulfur is yellow, and the explicit hydrogen is white. All other hydrogen atoms are treated implicitly.

EAM parameters from Bhattarai *et al.* for gold in polarizable systems.[S10] The damped shifted force model from Fennell and Gezelter was used for long-range electrostatic interactions with a damping parameter, $\alpha = 0.18$ Å^{-1}, which yields good agreement with Ewald electrostatics when $r_{\text{cut}} = 12$ Å.[S11]

Table S1: Non-bonded interactions used for simulations of gold nanostructures and thiolated PEG in a water solvent. All parameters listed are Lennard-Jones $n-m$ pairwise terms. The $\varepsilon_{\mathrm{Au}-i}$ values for water have been modified from Dou *et al.*[S12] to more closely replicate the adsorption energy for water on a (111) gold surface determined by DFT calculations.[S8] The cross interactions containing HO and H-SPCE are purely repulsive.

Atom	Mass (au)	σ_{ii} (Å)	ε_{ii} (kcal/mol)	$\sigma_{\mathrm{Au}-i}$ (Å)	$\varepsilon_{\mathrm{Au}-i}$ (kcal/mol)	n	m	Charge (e)	Source
Au	196.97	-	-	-	-	-	-	0.0	
CH2	14.03	3.95[a]	0.0914[a]	3.54[b]	0.175[b]	12	6	0.250[a]	Refs. S1[a], S3[b]
CH2OH	14.03	3.95[a]	0.0914[a]	3.54[b]	0.175[b]	12	6	0.265[a]	Refs. S1[a], S3[b]
CH2S	14.03	3.95[a]	0.0914[a]	3.54[b]	0.175[b]	12	6	0.171[a]	Refs. S2[a], S3[b]
OH	15.9994	3.02[a]	0.1848[a]	3.12[a,b]	0.213[a,b]	12	6	-0.700[a]	Refs. S1[a], S3[b]
HO	1.0079	0.0	0.0	1	79487.7[a]	12	-	0.435[a]	Ref. S1
OC	15.9994	2.80[a]	0.1093[a]	3.01[a,b]	0.164[a,b]	12	6	-0.500[a]	Refs. S1[a], S3[b]
S	32.0655	3.62[a]	0.4610[a]	2.65[b]	5.554[b]	12	6	-0.171[a]	Refs. S2[a], S13[b]
O−SPCE	15.9994	3.16549[a]	0.15532[a]	3.18284	0.6285748	9	6	-0.848	Refs. S14, S15
H−SPCE	1.0079	0.0	0.0	1	0.0008492	4	-	0.424	Refs. S14, S15

Table S2: Repulsive soft sphere (r^{-12}) interaction between the hydroxyl hydrogen and non-terminal ether oxygen (OC) atoms in the thiolated PEG.

i	j	σ_{ij} (Å)	ε_{ij} (kcal/mol)	n	Source
HO	OC	1	79487.7	12	Ref. S1

Table S3: Harmonic bond parameters for thiolated PEG. Water is simulated as a rigid body so no harmonic bond parameters are needed.

i	j	r_0 (Å)	K_{ij} (kcal/mol $\times$ Å^2)	Source
CH2	OC	1.41[a]	640.0[b]	Refs. S1[a], S4[b]
CH2	CH2	1.54[a]	536.0[b]	Refs. S1[a], S16[b]
CH2	CH2S	1.54[a]	536.0[b]	Refs. S1[a], S16[b]
OH	HO	0.945[a]	553.0[b]	Refs. S6[a], S4[b]
S	CH2S	1.81	444.0	Ref. S4
CH2OH	CH2	1.54[a]	536.0[b]	Refs. S1[a], S16[b]
OH	CH2OH	1.41[a]	640.0[b]	Refs. S1[a], S4[b]

Table S4: Harmonic bend parameters for thiolated PEG. The central atom in each bend is atom *j*, bonded to atoms *i* and *k*.

i	j	k	θ_0 (degrees)	K_{ijk} (kcal/mol $\times$ rad^2)	Source
HO	OH	CH2OH	108.5	110.0844	Ref. S6
CH2	CH2	OC	112.0	99.9503	Ref. S1
CH2	OC	CH2	112.0	120.0198	Ref. S1
CH2	CH2S	S	114.7	100.0	Ref. S2
OH	CH2OH	CH2	109.5	100.1490	Ref. S6
CH2OH	CH2	OC	112.0	99.9503	Ref. S1
OC	CH2	CH2S	112.0	99.9503	Ref. S2

Table S5: TraPPE torsions for thiolated PEG which have the form $V_{\text{torsion}}(\phi) = c_0 + c_1(1 + \cos\phi) + c_2(1 - \cos 2\phi) + c_3(1 + \cos 3\phi)$.

i	j	k	l	c_0	c_1	c_2	c_3	Source
CH2	CH2OH	OH	HO	0.0	0.4169	-0.0580	0.3734	Ref. S6
CH2	CH2	OC	CH2	0.0	1.4413	-0.3254	1.1092	Ref. S1
OC	CH2	CH2	OC	1.0	0.0	-0.500	2.0	Ref. S1
S	CH2S	CH2	OC	1.0	0.0	-0.500	2.0	Ref. S2
OH	CH2OH	CH2	OC	1.0	0.0	-0.500	2.0	Ref. S1
CH2OH	CH2	OC	CH2	0.0	1.441	-0.325	1.109	Ref. S2
CH2	OC	CH2	CH2S	0.0	1.441	-0.325	1.109	Ref. S2

Table S6: Gold EAM parameters for $\phi(r)$ and $f(r)$. $\phi(r)$ is a generalized elemental pair potential. The electron density function $f(r)$ has the same form as the attractive portion of $\phi(r)$.

$$\phi(r) = \frac{\mathbf{A}\mathbf{exp}[-\alpha(\frac{r}{r_e}-1)]}{1+(\frac{r}{r_e}-\kappa)} - \frac{\mathbf{B}\mathbf{exp}[-\beta(\frac{r}{r_e}-1)]}{1+(\frac{r}{r_e}-\lambda)^{20}};$$

$$f(r) = \frac{f_e\mathbf{exp}[-\beta(\frac{r}{r_e}-1)]}{1+(\frac{r}{r_e}-\lambda)^{20}}.$$

r_e(Å)	f_e(eV/Å)	ρ_e(eV/Å)	ρ_s(eV/Å)	α	β	A	B	κ	λ	Source
2.885034	1.529021	19.991632	19.991509	9.516052	5.075228	0.229762	0.356666	0.35657	0.748798	Ref. S9

Table S7: Gold EAM parameters for the embedding function $F(\rho)$. The three equations below allow the calculation of $F(\rho)$ at three different electron density ranges:

$F(\rho) = \sum_{i=0}^{3} F_{ni}(\frac{\rho}{\rho_n} - 1)^i$, $\rho < \rho_n, \rho_n = 0.85\rho_e$;

$F(\rho) = \sum_{i=0}^{3} F_i(\frac{\rho}{\rho_e} - 1)^i$, $\rho_n \leq \rho < \rho_0, \rho_0 = 1.15\rho_e$;

$F(\rho) = F_e[1 - ln(\frac{\rho}{\rho_s})^\eta](\frac{\rho}{\rho_s})^\eta$, $\rho < \rho_n, \rho_0 \leq \rho$.

F_{n0}	F_{n1}	F_{n2}	F_{n3}	F_0	F_1	F_2	F_3	F_e	η	Source
– 2.937772	-0.500288	1.601954	-0.835530	-2.98	0	1.706587	-1.134778	-2.978815	1.021095	Ref. S9

Table S8: Gold DR-EAM self-potential parameters. The chargeMass term is a tunable parameter that determines the speed at which the polarizable gold atom responds to an external field. $N_{\mathbf{eff}}$ describes the effective number of charge carriers per gold atom. All parameter units result in a self-potential in eV. The self-potential is described by $V_{self}(q) = \sum_{n=1}^{6} a_n q^n$.

chargeMass	N_{eff}	a_1	a_2	a_3	a_4	a_5	a_6	Source
1000.0	0.59	13.89	7.92	13.192055	68.173897	-88.029873	28.855093	Ref. S10

System Preparation and Equilibration

Planar gold slabs ($a = 4.08$Å) exposing the (111), (110), and (100) facets were built with slabBuilder, an OpenMD utility that rotates the specified facet so that it is positioned normal to the z-axis of the simulation cell.[S17] An identically-sized solvent box was constructed using Packmol[S18] and OpenMD,[S17] and the thiolated PEG positions were randomized in each statistically-independent replica (with four replicas for each studied interface).

The spherical gold nanoparticles used in all non-periodic simulations were built with a lattice constant of 4.08 Å using nanoparticleBuilder, another OpenMD utility.[S17] These particles were constructed with a radius of either 10 or 20 Å. The gold nanoparticle underwent structural relaxation with incremental temperature increases up to 300 K. The solvent spheres were created with empty center regions to allow for simplified merging with the gold nanoparticles. One gold atom at the center of the spherical nanoparticle was given a large mass ($m = 1.9697 \times 10^6$ amu) to prevent nanoparticle drifting.

For all systems, the metal and solvent layers were combined using other OpenMD utilities, and steepest descent optimization was used to structurally relax each system. Particle velocities were resampled from a Maxwell-Boltzmann distribution at 300 K prior to equilibration.[S17] The structural makeup of each system studied is shown in Table S9.

All systems using the DR-EAM metal potential were simulated directly prior to equilibration using a time step of 0.2 fs, as the charge degrees of freedom in DR-EAM must be simultaneously propagated. A time step of 1 fs was used for all equilibration and flux application steps.

Table S9: Structures simulated in this work

	Spheres		Slabs		
	10 Å	20 Å	(111)	(110)	(100)
Metallic structure (in Å)	$r = 10$	$r = 20$	$31 \times 36 \times 28$	$30 \times 35 \times 29$	$30 \times 36 \times 29$
Total System size (in Å)	$r \sim 40$	$r \sim 50$	$31 \times 36 \times 117$	$30 \times 35 \times 120$	$30 \times 36 \times 118$
Gold volume (Å^3)	4,189	33,510	29,340	28,525	28,525
Solvent volume (Å^3)	175,406	490,088	101,250	97,900	101,030
N_{Gold}	249	1985	1728	1680	1680
N_{Water}	6018	17,024	2854	2790	2790
$N_{\text{thiolatedPEG}}$	59	234	104	98	100
$\rho_{\text{thiolatedPEG}}$ (nm^{-2})	4.70	4.66	4.81	4.67	4.63

The planar systems were first structurally relaxed (NVT), followed by a pressure correction (NPT) with separate barostats for each dimension. This was followed by thermal relaxation (NVT) and equilibration using a microcanonical integrator (NVE). The planar systems were simulated using periodic boundary conditions. The spherical systems were equilibrated for 250 ps using the non-periodic Langevin Hull integrator[S19] and velocity resampling at 300 K every ps, and then an additional 200 ps with no resampling.

After equilibration, a thermal flux was applied to each system using the velocity shearing and scaling reverse non-equilibrium molecular dynamics (VSS-RNEMD) methods developed by Kuang and Gezelter.[S20] A flux was applied until thermal gradients and temperature discontinuities developed. Kinetic energy was exchanged between either two slabs separated in z (planar systems) or two concentric spherical shells (spherical systems). The thermal flux was applied for 5 ns in all systems. For planar systems, the thermal data shown in this work was averaged across the entire 5 ns of flux application. For the nanospheres, the thermal data was averaged across the last 1 ns of flux application. Coupling to the thermal bath was removed in spherical systems so as to prevent interference with the applied flux. In polarizable systems, the fluctuating charges were propagated using a microcanonical (NVE) integrator to mitigate unphysical losses of kinetic energy into the electronic degrees of freedom.

In Figure S2, we show that we are in the linear response regime with the applied flux utilized in the main paper. We tested a total of five flux values, and these were applied for 5 ns on a set of Au(111) systems. The flux used for planar systems in this work was 5.0×10^{-6} kcal $\text{mol}^{-1}\text{Å}^{-2}$ fs^{-1} (3500 MW m^{-2}).

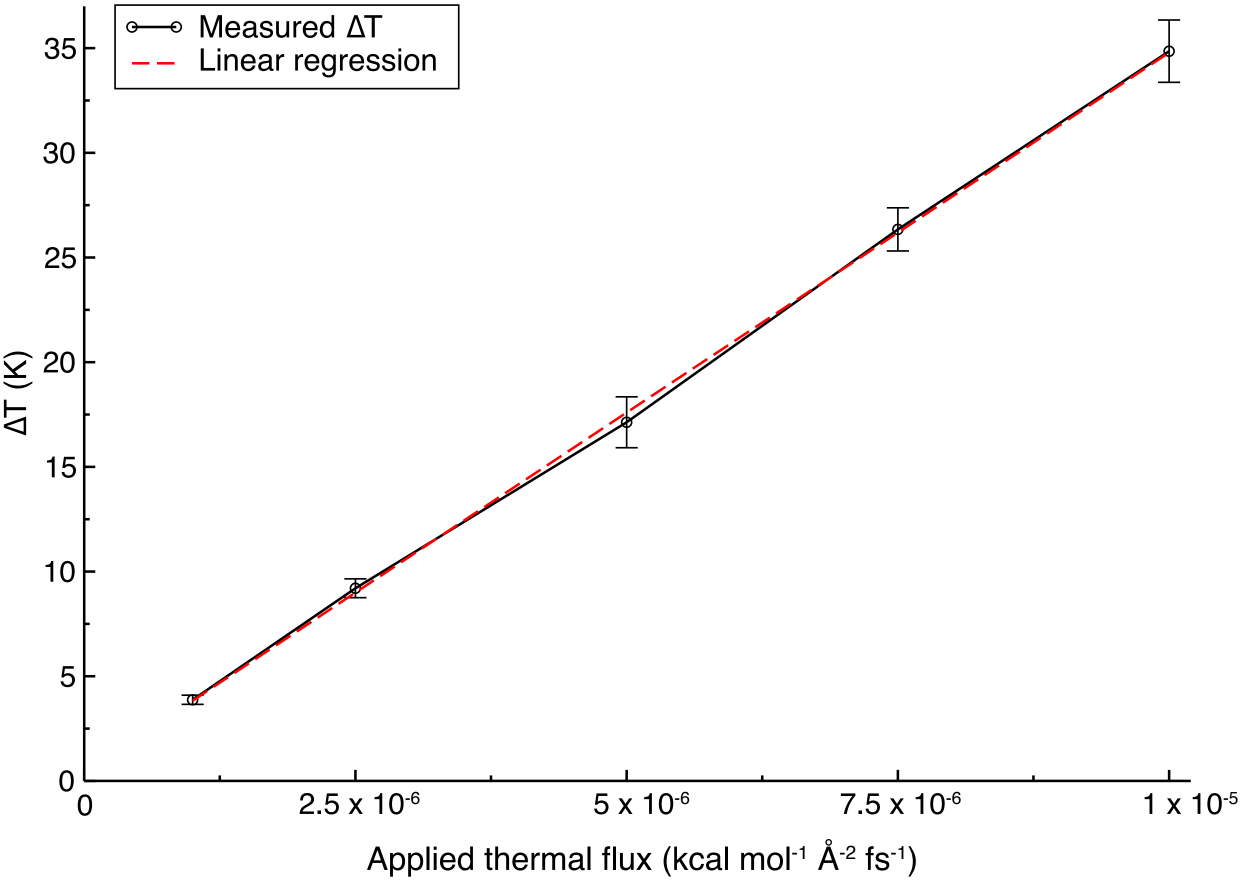

Figure S2: A test of five values of applied flux bracketing the flux used in the main paper. This test is for Au(111) interfaces. Each point is an average of four statistically independent simulations.

Additional Thermal Profiles and Mass Densities

The thermal profiles and local mass densities for all components in polarizable systems are shown in Figures S3 and S4. The temperature drop is largest between gold and sulfur in these systems as in their non-polarizable counterparts. There are no compelling differences between Figure S3 and Figure 2 in the main text, but we note a small decrease in the penetration of sulfur into gold in the polarizable Au(111) surface. The ordering of water molecules near the interface are similar to that of Figure 2. When comparing Figure S4 with Figure 3 in the main text, it is clear that polarizability makes no significant difference in the ordering of any species.

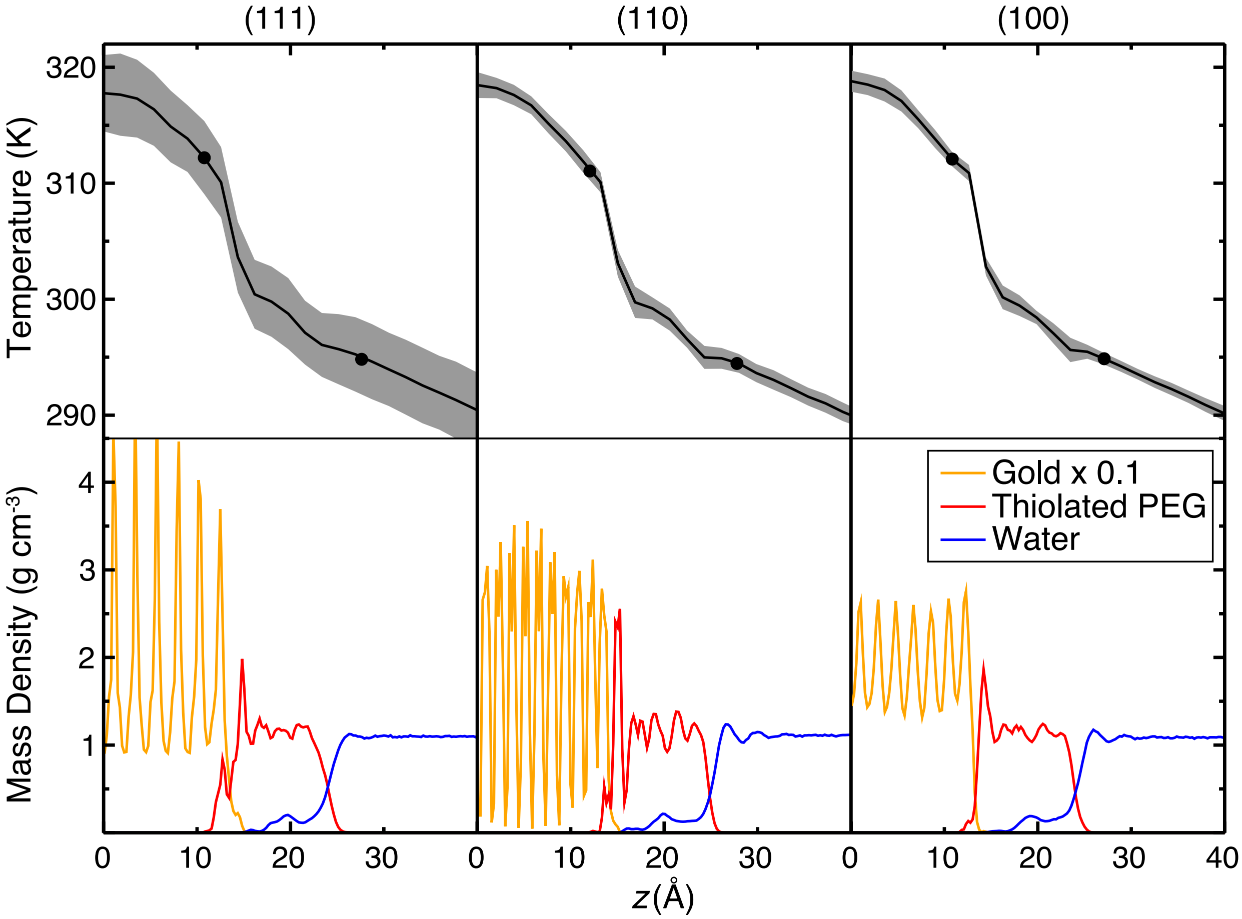

Figure S3: Under an applied thermal flux, temperature drops are largest at the location of the Gold-Sulfur bond. (Top) Thermal profiles of planar systems simulated using the polarizable DR-EAM potential. Shading indicates the 95% confidence interval for computed temperatures, while the black dots are the bounds of the interfacial region used for computing conductance. (Bottom) Mass densities of each species. $z = 0$ represents the center of the gold slabs.

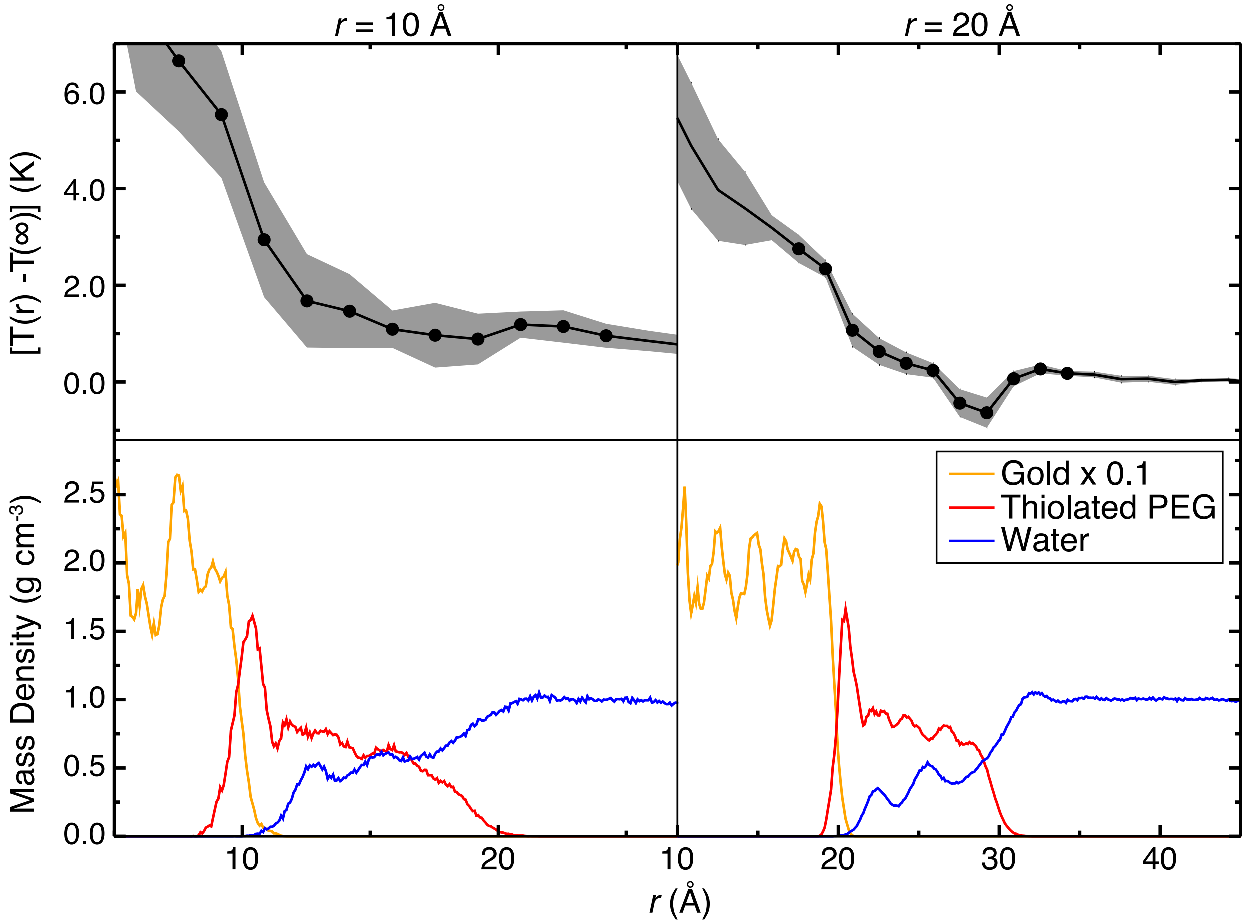

Figure S4: In the nanospheres, temperature drops are also largest at the Gold-Sulfur bond. (Top) Thermal profiles of nanoparticle systems, relative to the temperature of the solvent far from the particle. The shaded region represents the 95% confidence intervals. The black data points are the temperature differences in the Kapitza region which were used for calculating conductance. (Bottom) Local mass densities of each species for the nanoparticles using the polarizable DR-EAM model. $r = 0$ is at the center of the gold nanosphere.

Additional Vibrational Power Spectra

The vibrational power spectra for all components of the planar systems are shown in Figure S5. There are no clear differences across metallic facet or polarizability here. The full gold spectra cannot be seen here, but they do not differ significantly and obscure the other spectra when in full view.

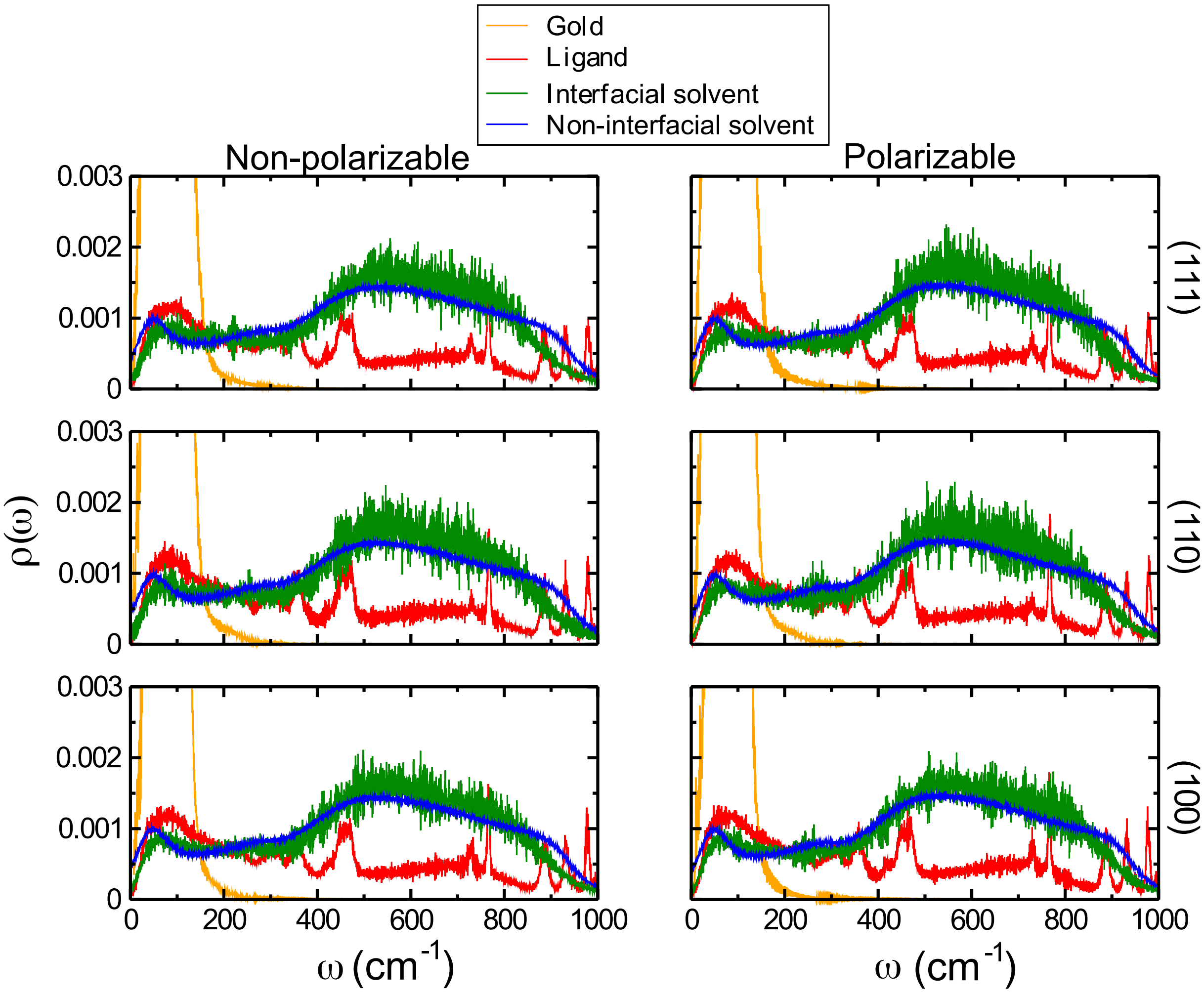

Figure S5: Low frequency portions of the vibrational power spectra for all planar systems studied. Note that the y-axis has been scaled down to allow visualization of the ligand and solvent spectra, and the gold spectra extend beyond the scope of these plots.

The vibrational power spectra for all components of spherical systems are shown in Figure S6. There appears to be little effect of either system size or metal polarizability here as well. Again, the gold spectra do not differ significantly and are thus not fully shown. A full analysis of the differences in spectra between the planar and spherical systems is available in the main text.

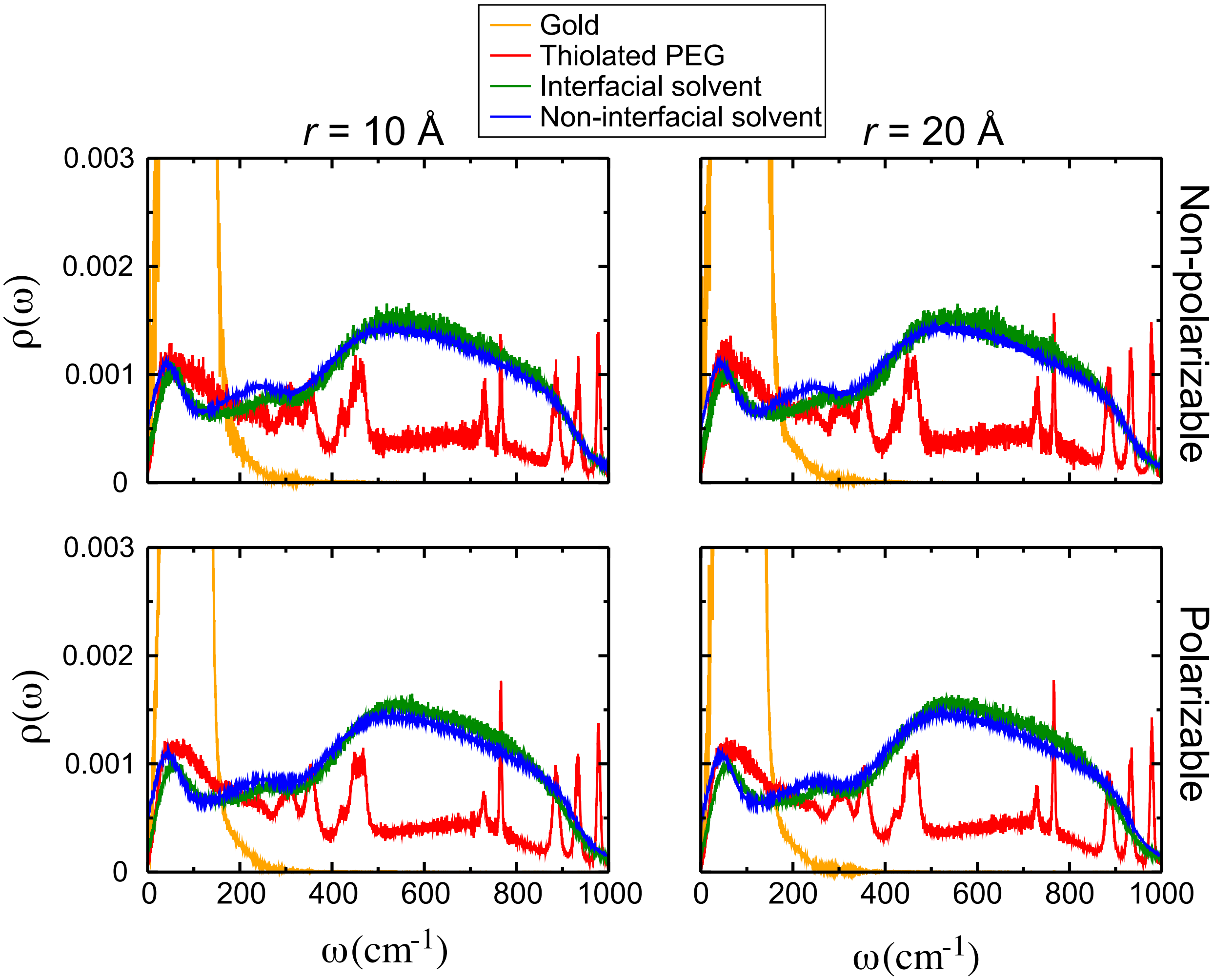

Figure S6: Vibrational power spectra for all spherical systems studied. The y-axis has been scaled as in Fig. S5.

As thiolated PEG exhibits both low and high frequency activity, we have computed the averaged spectra for thiolated PEG in the planar and nanosphere systems which are are shown in Figure S7. Overall, these spectra do not differ significantly. The peak ranging from approximately 3700 - 3900 cm^{-1} is likely an O-H stretch from the terminal hydroxyl group.

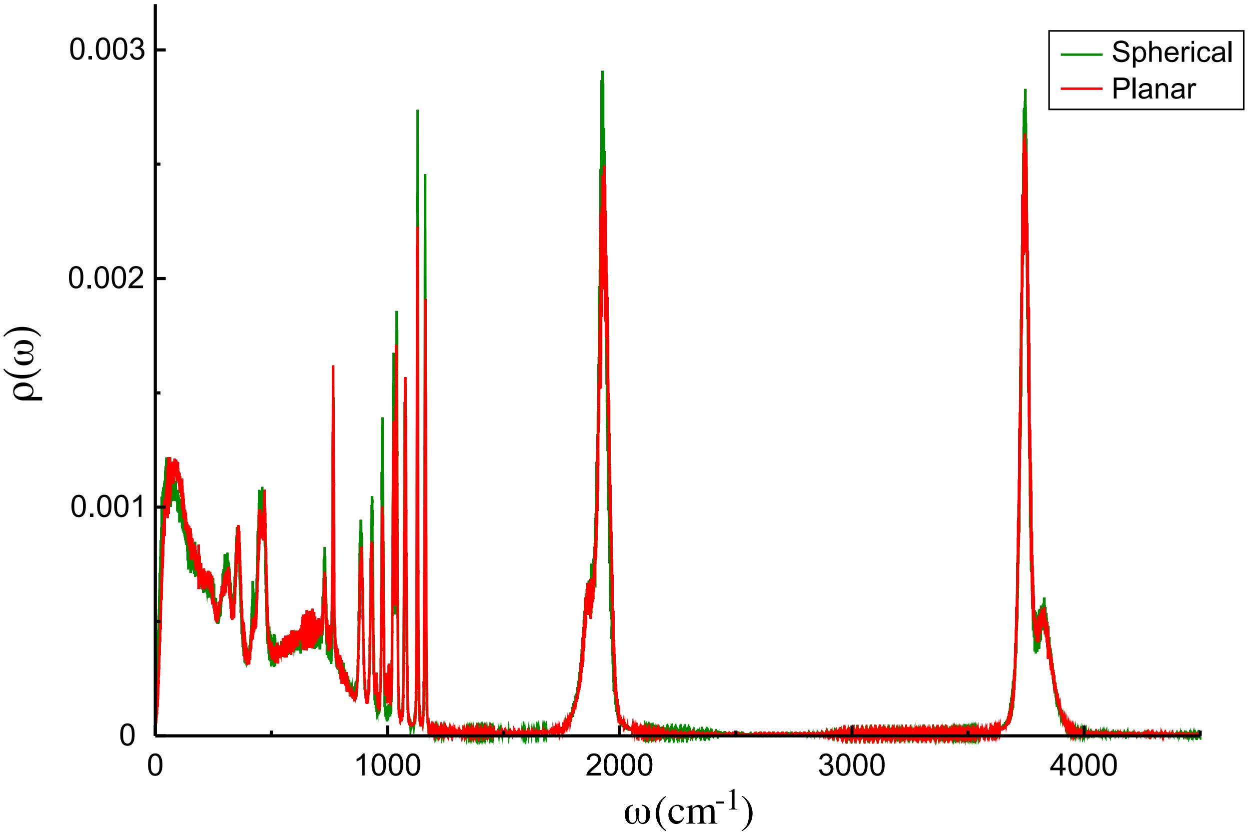

Figure S7: Averaged thiolated PEG vibrational power spectra for planar and spherical systems. Note: the planar curve is an average of all polarizable and non-polarizable (111), (110), and (100) facets, and the spherical curve is an average of all polarizable and non-polarizable nanospheres with radii of 10 and 20 Å.

Additional Bhattacharyya Coefficients

We have also included Bhattacharyya coefficients (BC) which are similar calculations to those in Table 3 but using power spectra rather than mass densitites. The BC values for the thiolated PEG / gold and thiolated PEG / water pairs are shown in Table S10. The water has been categorized into interfacial and bulk regions, where interfacial water comprises solvent molecules that are trapped in the thiolated PEG layer, and bulk water captures the solvent molecules outside that region. The magnitude of BC values are larger for each pair here than those for the same pairs calculated with mass densities. These coefficients appear to be unaffected by metallic polarizability or planar facet, but the mean BC values for the thiolated PEG / gold pair are higher in the 10 Å nanospheres than for the other systems. As expected, there is very little difference between the BCs for bulk and interfacial water, and their power spectra exhibit a significant amount of overlap with that of thiolated PEG. In Table 3, we noted that the BCs for the thiolated PEG-gold pair in the Au(111) systems were about twice as large as those for the Au(110) and Au(100) systems, but that difference does not exist here.

Table S10: Vibrational power spectral overlap measured using Bhattacharyya coefficients, showing the degree of similarity between the thiolated PEG and the other two components of the metal / ligand / water systems.

Facet	Metal	BC with thiolated PEG (unitless)		
		Interfacial water	Bulk water	Gold
(111)	non-polarizable	0.740 ± 0.007	0.737 ± 0.007	0.434 ± 0.007
	polarizable	0.732 ± 0.008	0.741 ± 0.014	0.447 ± 0.013
(110)	non-polarizable	0.737 ± 0.011	0.745 ± 0.007	0.438 ± 0.018
	polarizable	0.735 ± 0.009	0.735 ± 0.002	0.426 ± 0.006
(100)	non-polarizable	0.747 ± 0.007	0.747 ± 0.004	0.424 ± 0.013
	polarizable	0.736 ± 0.007	0.739 ± 0.007	0.423 ± 0.015
NP ($r = 10$ Å)	non-polarizable	0.739 ± 0.015	0.740 ± 0.014	0.452 ± 0.022
	polarizable	0.740 ± 0.011	0.740 ± 0.013	0.452 ± 0.016
NP ($r = 20$ Å)	non-polarizable	0.745 ± 0.004	0.745 ± 0.004	0.429 ± 0.008
	polarizable	0.741 ± 0.005	0.742 ± 0.004	0.427 ± 0.006

Charge Penetration at the Interface

The image charge effect describes the phenomenon in which a metallic species responds to a nearby external charge by inducing the opposite charge on its surface. DR-EAM has previously been shown to replicate this effect in systems of bare gold solvated in water.[S7,S10] To investigate how these systems respond when the gold is polarizable, we calculated the charge density as a function of *z* (for planar systems) or *r* (for spherical systems).

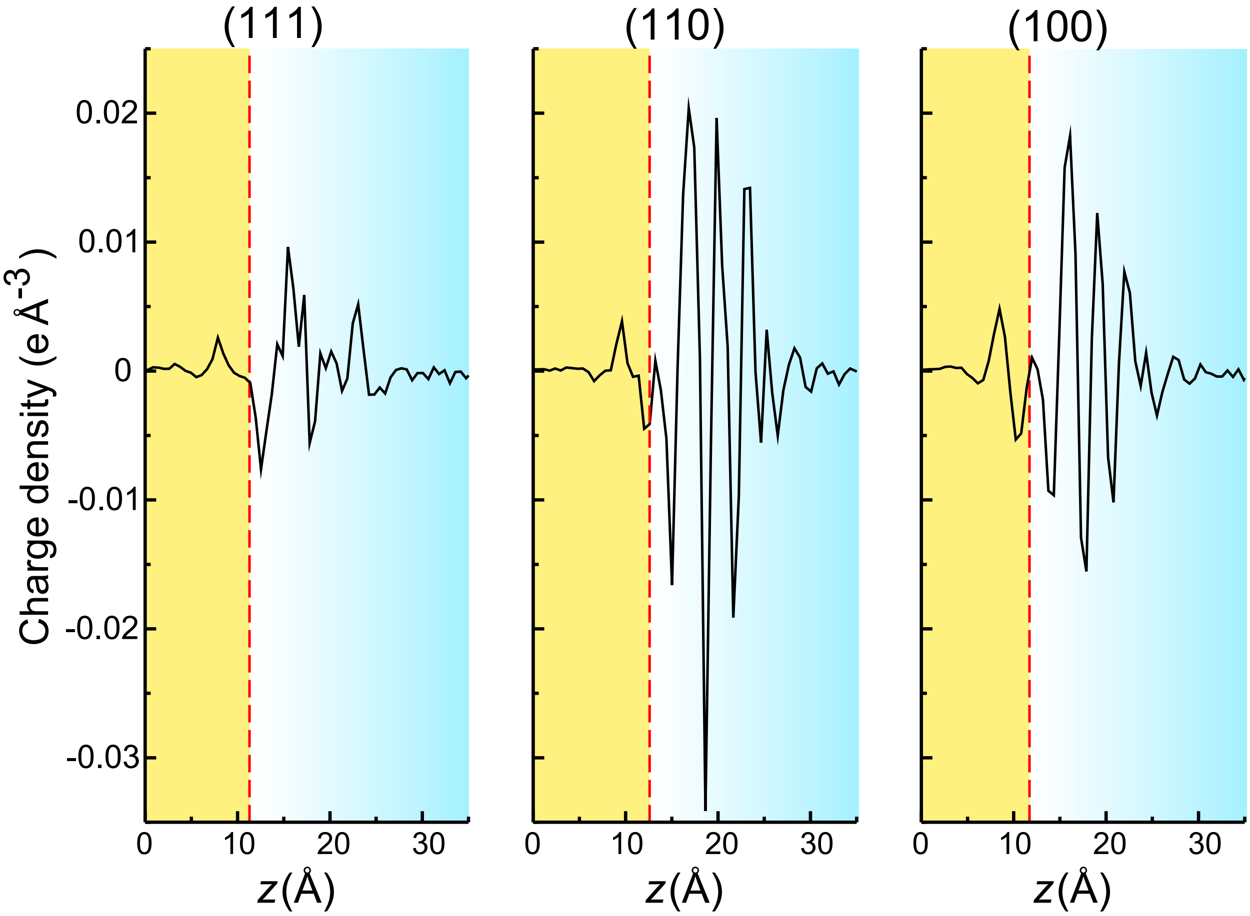

Figure S8: Charge density as a function of *z* in planar systems using the polarizable metal potential DR-EAM. The dashed red line indicates the gold/thiolated PEG interface in each plot.

Figure S8 shows the charge density as a function of *z* for planar systems. The positive peak directly to the left of the interface on each plot (dashed red line) represents the positive charge of the surface gold atoms responding to the negatively charged sulfur atoms near the surface. The magnitude of these peaks does not vary significantly, suggesting that the difference in gold atom packing across fcc lattices does not change the ordering of charges at the gold surface. The negative peak directly adjacent to the gold represents the sulfur atoms in the thiolated PEG molecules. Unlike the gold peaks, these vary across gold facets, as does the magnitude of the ether oxygen peaks starting at around 20 Å. This difference in the gold surface disruption likely leads to the differing magnitudes of sulfur and ether oxygen peaks. It is also clear from these plots that the ligand layer is more ordered on the Au(110) and Au(100) facets.

The charge density as a function of r is shown for spherical systems in Figure S9. Here, the magnitude of the first gold peak is approximately equal in both systems, as is the sulfur peak. However, the magnitude of the second gold peak differs greatly, with a much larger magnitude in the smaller systems. Additionally, the ether oxygens appear to be more ordered in systems where the gold radius is 20 Å, with clear ordering out to $r = 30$ Å, the approximate location of the hydroxyl oxygen. In the smaller nanospheres, the thiolated PEG chains have more internal disorder, and the ether oxygen minima are discernible only out to $r = 15$ Å.

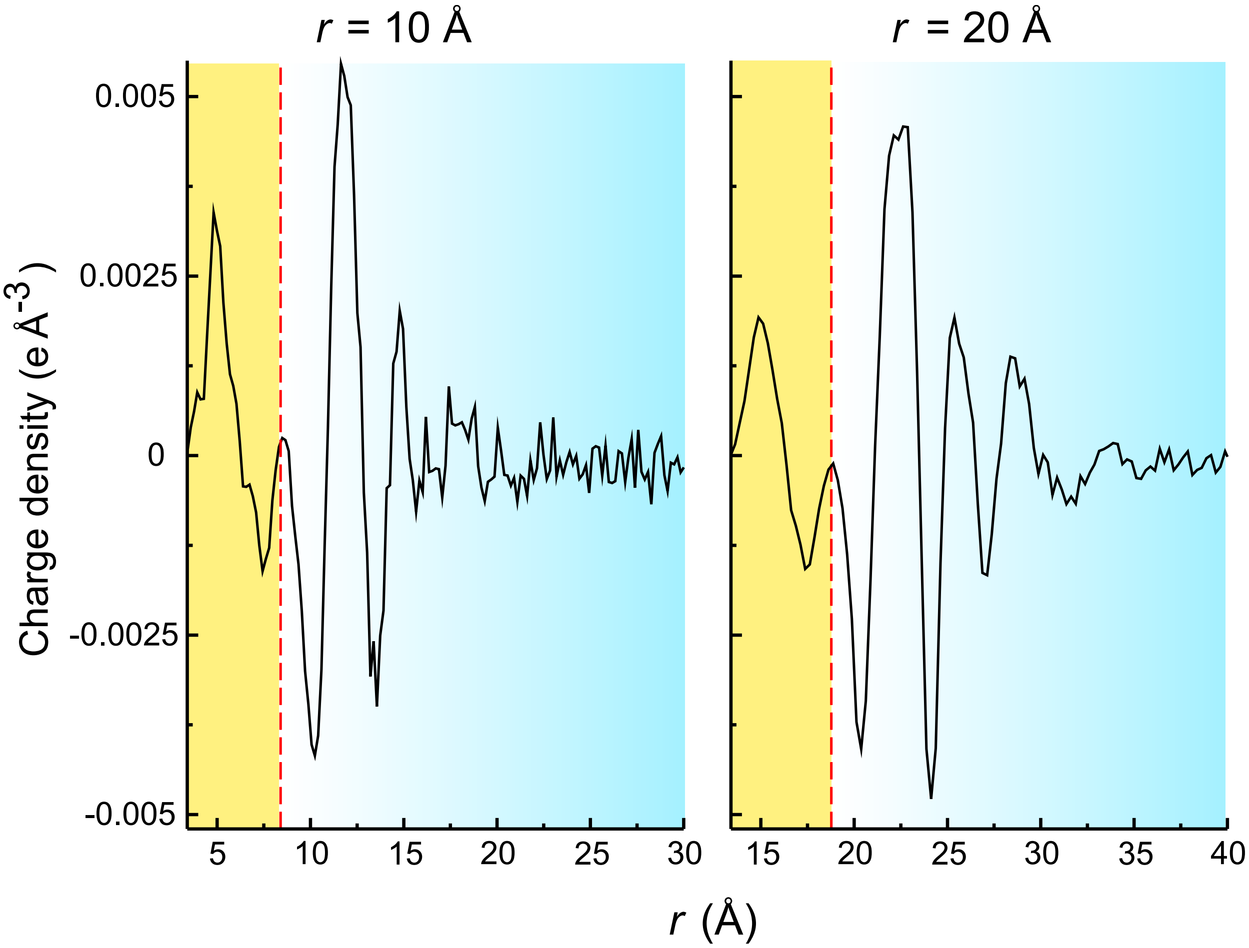

Figure S9: Charge density as a function of *r* in spherical systems using the polarizable metal potential DR-EAM.

References

(S1) Stubbs, J. M.; Potoff, J. J.; Siepmann, J. I. Transferable Potentials for Phase Equilibria. 6. United-Atom Description for Ethers, Glycols, Ketones, and Aldehydes. *J. Phys. Chem. B* **2004**, *108*, 17596–17605.

(S2) Lubna, N.; Kamath, G.; Potoff, J. J.; Rai, N.; Siepmann, J. I. Transferable Potentials for Phase Equilibria. 8. United-Atom Description for Thiols, Sulfides, Disulfides, and Thiophene. *J. Phys. Chem. B* **2005**, *109*, 24100–24107.

(S3) Schapotschnikow, P.; Pool, R.; Vlugt, T. J. H. Selective adsorption of alkyl thiols on gold in different geometries. *Comp. Phys. Comm.* **2007**, *177*, 154–157.

(S4) Weiner, S. J.; Kollman, P. A.; Nguyen, D. T.; Case, D. A. An all atom force field for simulations of proteins and nucleic acids. *J. Comp. Chem.* **1986**, *7*, 230–252.

(S5) Martin, M. G.; Siepmann, J. I. Transferable Potentials for Phase Equilibria. 1. United-Atom Description of n-Alkanes. *J. Phys. Chem. B* **1998**, *102*, 2569–2577.

(S6) Chen, B.; Potoff, J. J.; Siepmann, J. I. Monte Carlo Calculations for Alcohols and Their Mixtures with Alkanes. Transferable Potentials for Phase Equilibria. 5. United-Atom Description of Primary, Secondary, and Tertiary Alcohols. *J. Phys. Chem. B* **2001**, *105*, 3093–3104.

(S7) Shavalier, S. A.; Gezelter, J. D. Thermal Transport in Citrate-Capped Interfaces Using a Polarizable Force Field. *J. Phys. Chem. C* **2022**, *126*, 12742–12754.

(S8) Berg, A.; Peter, C.; Johnston, K. Evaluation and Optimisation of Interface Force Fields for Water on Gold Surfaces. *J. Chem. Theory Comput.* **2017**, *13*, 5610–5623.

(S9) Zhou, X.; Johnson, R.; Wadley, H. Misfit-energy-increasing dislocations in vapor-deposited CoFe/NiFe multilayers. *Phys. Rev. B* **2004**, *69*, 144113.

(S10) Bhattarai, H.; Newman, K.; Gezelter, J. Polarizable potentials for metals: The density readjusting embedded atom method (DR-EAM). *Phys. Rev. B* **2019**, *99*, 094106.

(S11) Fennell, C.; Gezelter, J. Is the Ewald summation still necessary? Pairwise alternatives to the accepted standard for long-range electrostatics. *J. Chem. Phys.* **2006**, *124*, 234104.

(S12) Dou, Y.; Zhigilei, L. V.; Winograd, N.; Garrison, B. J. Explosive Boiling of Water Films Adjacent to Heated Surfaces: A Microscopic Description. *J. Phys. Chem. A* **2001**, *105*, 2748–2755.

(S13) Pool, R.; Schapotschnikow, P.; Vlugt, T. J. H. Solvent Effects in the Adsorption of Alkyl Thiols on Gold Structures: A Molecular Simulation Study. *J. Phys. Chem. C* **2007**, *111*, 10201–10212.

(S14) Berendsen, H.; Grigera, J.; Straatsma, T. The Missing Term in Effective Pair Potentials. *J. Phys. Chem.* **1987**, *91*, 6269–6271.

(S15) Bhattarai, H.; Newman, K.; Gezelter, J. The role of polarizability in the interfacial thermal conductance at the gold-water interface. *J. Chem. Phys.* **2020**, *153*, 204703.

(S16) Jorgensen, W. L.; Maxwell, D. S.; Tirado-Rives, J. Development and Testing of the OPLS All-Atom Force Field on Conformational Energetics and Properties of Organic Liquids. *J. Am. Chem. Soc.* **1996**, *118*, 11225–11236.

(S17) Gezelter, J.; Bhattarai, H.; Drisko, C.; Duraes, A.; Lin, T.; Vardeman, C.; Fennell, C.; Meineke, M.; Louden, P.; Neidhart, S.; Kuang, S.; Lamichhane, M.; Michalka, J.; Stocker, K.; Marr, J.; Sun, X.; Li, C.; Daily, K.; Zheng, Y. *OpenMD, an Open Source Engine for Molecular Dynamics*, Version 2.7; http://openmd.org. Accessed December 2, 2022.

(S18) Martínez, L.; Andrade, R.; Birgin, E.; Martínez, J. Packmol: A package for building initial configurations for molecular dynamics simulations. *J. Chem. Comput.* **2009**, *30(13)*, 2157–2164.

(S19) Vardeman, C. F.; Stocker, K. M.; Gezelter, J. D. The Langevin Hull: Constant Pressure and Temperature Dynamics for Nonperiodic Systems. *J. Chem. Theory Comput.* **2011**, *7*, 834–842.

(S20) Stocker, K. M.; Gezelter, J. D. Simulations of Heat Conduction at Thiolate-Capped Gold Surfaces: The Role of Chain Length and Solvent Penetration. *J. Phys. Chem. C* **2013**, *117*, 7605–7612.